

Effects of Magnetic Fields on Gas Dynamics and Star Formation in Nuclear Rings

SANGHYUK MOON ^{1,2} WOONG-TAE KIM ^{1,3} CHANG-GOO KIM ² AND EVE C. OSTRIKER ²

¹*Department of Physics & Astronomy, Seoul National University, Seoul 08826, Republic of Korea*

²*Department of Astrophysical Sciences, Princeton University, Princeton, NJ 08544, USA*

³*SNU Astronomy Research Center, Seoul National University, Seoul 08826, Republic of Korea*

ABSTRACT

Nuclear rings at the centers of barred galaxies are known to be strongly magnetized. To explore the effects of magnetic fields on star formation in these rings and nuclear gas flows, we run magnetohydrodynamic simulations in which there is a temporally-constant magnetized inflow to the ring, representing a bar-driven inflow. The mass inflow rate is $1 M_{\odot} \text{ yr}^{-1}$, and we explore models with a range of field strength in the inflow. We adopt the TIGRESS framework developed by Kim & Ostriker to handle radiative heating and cooling, star formation, and resulting supernova (SN) feedback. We find that magnetic fields are efficiently amplified in the ring due to rotational shear and SN feedback. Within a few 100 Myr, the turbulent component B_{trb} in the ring saturates at $\sim 35 \mu\text{G}$ (in rough equipartition with the turbulent kinetic energy density), while the regular component B_{reg} exceeds $50 \mu\text{G}$. Expanding superbubbles created by clustered SN explosions vertically drag predominantly-toroidal fields from near the midplane to produce poloidal fields in high-altitude regions. The growth of magnetic fields greatly suppresses star formation at late times. Simultaneously, strong magnetic tension in the ring drives radially inward accretion flows from the ring to form a circumnuclear disk in the central region; this feature is absent in the unmagnetized model.

1. INTRODUCTION

A characteristic result of dynamical interactions between a bar and gas in disk galaxies is the formation of a pair of large-scale shocks running along the leading sides of the bar inside of corotation. Gas entering the shock front loses angular momentum and is deflected inward. In optical images, the compressed inflowing gas is seen as narrow dust lanes along which gas is funnelled toward the central regions. The observed mass inflow rate is of the order of $\dot{M}_{\text{in}} \sim 0.1\text{--}10 M_{\odot} \text{ yr}^{-1}$ and is believed to be time-variable (Benedict et al. 1996; Regan et al. 1997; Meier et al. 2008; Elmegreen et al. 2009; Shimizu et al. 2019; Sormani & Barnes 2019).

Bar-driven inflowing gas has residual angular momentum and thus forms a circumnuclear ring, which is often observed to be active in star formation. Star-forming nuclear rings are found in about $\sim 20\%$ of disk galaxies in the local universe, 80% among which are barred (Comerón et al. 2010), and have star formation rates (SFRs) of $\sim 0.1\text{--}10 M_{\odot} \text{ yr}^{-1}$ (Mazzuca et al. 2008; Ma

et al. 2018). While nuclear rings are sometimes found in unbarred galaxies, a majority of such galaxies have oval distortions, strong spiral arms, or close companions, all of which are thought to provide non-axisymmetric gravitational torques similar to bars that could effectively drive gas inward (Comerón et al. 2010). Spectroscopic observations have revealed that nuclear rings are long-lived, composed of not only young star clusters formed recently but also old stellar populations with ages ranging from ~ 100 Myr to a few Gyrs. The reconstructed star formation histories are characterized by a large time variability, involving multiple timescales ranging from a few tens of Myrs to a few Gyrs (e.g., Allard et al. 2006; Sarzi et al. 2007; Gadotti et al. 2019; Prieto et al. 2019; Nogueras-Lara et al. 2020). Over time, ring star formation may lead to the development of nuclear disks (Launhardt et al. 2002; Bittner et al. 2020; Gadotti et al. 2020; de Sá-Freitas et al. 2022; Sormani et al. 2022), which are also known as “disk-like bulges” as distinct from classical and box/peanut bulges (Athanasoula 2005).

Recently, a number of authors have studied gas dynamics and star formation in and around nuclear rings, using numerical simulations with realistic treatment of star formation and feedback. For example, Armillotta et al. (2019) conducted hydrodynamic simulations of

sanghyuk.moon@princeton.edu, unitree@snu.ac.kr

cgkim@astro.princeton.edu, eco@astro.princeton.edu

the interstellar medium (ISM) to study gas flows and star formation in the Central Molecular Zone (CMZ), which is believed to represent a nuclear ring in our own Milky Way. Their simulations (with a mass resolution of $2 \times 10^3 M_\odot$) showed that the SFR of the CMZ goes through several burst-quench cycles with a mixture of a short period (~ 50 Myr) and long period (~ 200 Myr), although the gas mass remains relatively constant over time. Tress et al. (2020) and Sormani et al. (2020) used a higher mass resolution of $< 100 M_\odot$ (with adaptive mass refinement depending on local density and temperature) to model the CMZ, resolving Sedov-Taylor blastwaves for most supernova (SN) explosions in their simulations. Contrary to Armillotta et al. (2019), these authors found that the SFR in the ring steadily increases in time in proportion to the gas mass, with the gas depletion time almost constant within a factor of ~ 2 . Seo et al. (2019) ran hydrodynamic simulations coupled with N -body stellar dynamics to study how a nuclear ring forms and evolves in a situation where a stellar bar forms and grows self-consistently, rather than being treated as a fixed potential. They found that star formation in a nuclear ring is sustained for a long (> 1 Gyr) period of time, and that the ring SFR correlates well with the mass inflow rate to the ring.

The diversity of findings from the above studies motivated us to undertake simulations with higher resolution in the ring region than it is possible to achieve with global models. A key goal was to test whether a constant mass inflow rate results in steady ring star formation, or if instead the gas mass builds up and then produces intermittent bursts of star formation. To explore whether steady vs. bursty behavior in ring star formation may depend on the inflow rate, in Moon et al. (2021) (hereafter Paper I) we developed a semi-global numerical framework that provides explicit control of the mass inflow rate via boundary conditions. Paper I found that, (1) when the mass inflow rate is fixed in time, a quasi-steady equilibrium state is reached at $\text{SFR} \sim 0.8 \dot{M}_{\text{in}}$ for a wide range of \dot{M}_{in} ($0.125\text{--}8 M_\odot \text{ yr}^{-1}$), in which the SFR and depletion time are almost constant within a factor of ~ 2 ; (2) vertical dynamical equilibrium is established within the ring gas, in which the thermal and turbulent pressures due to stellar feedback balance the gravitational field arising from both gas and stars; (3) the pressure-regulated, feedback-modulated (PRFM) star formation theory is satisfied as previously shown for featureless disks in Kim & Ostriker (2017) and Ostriker & Kim (2022), and for disks with a spiral arm potential in Kim et al. (2020), but in contrast to disk regions where the SFR adapts to the equilibrium value set by gas mass,

in nuclear rings the gas mass instead adapts to the SFR set by the mass inflow rate.

To understand what might have produced temporal variations as well as spatial asymmetry of observed ring star formation, and how the delay between star formation and feedback affects interpretation of self-regulated equilibrium, in Moon et al. (2022) (hereafter Paper II) we allowed the mass inflow rate to vary with time in a prescribed way and/or to be spatially asymmetric. Paper II found that (1) time-varying mass inflows with a sufficient oscillation amplitude cause episodic star formation, provided that the timescale of the inflow rate variations is sufficiently long ($\gtrsim 50$ Myr); (2) a sudden increase of the mass inflow rate through one of the two dust lanes causes lopsided star formation in the ring, lasting no longer than a few orbital period; (3) the PRFM theory is still satisfied even for a non-steady system in which the SFR and gas mass vary with time, provided that the time delay between star formation and feedback is properly taken into account.

While the studies above have improved our understanding of star-forming physics in nuclear rings, they were all limited to unmagnetized models. Observations show that nuclear rings in real galaxies are quite strongly magnetized. Assuming energy equipartition between magnetic fields and cosmic rays (CRs), the average magnetic field strengths in nuclear rings inferred from radio synchrotron observations are estimated to be $\sim 55 \mu\text{G}$ for NGC 1097 (Beck et al. 2005), $\sim 63 \mu\text{G}$ for NGC 1365 (Beck et al. 2005), and $\sim 84 \mu\text{G}$ for NGC 5792 (Yang et al. 2022), much stronger than in spiral arms of normal disk galaxies (Beck 2015). Beck et al. (1999, 2005) mapped radio continuum emission in barred galaxies and found that the magnetic fields are predominantly parallel to the dust lanes, while penetrating the nuclear rings with a large pitch angle ($\sim 40^\circ$). Strong magnetic fields would provide additional support for gas against gravity, potentially reducing the SFR (Pillai et al. 2015; Tabatabaei et al. 2018). Indeed, Tabatabaei et al. (2018) found a strong positive correlation between the gas depletion time and the magnetic field strength for individual giant clumps distributed along the nuclear ring of NGC 1097. No correlation was found between the depletion time and the turbulent velocity dispersion, suggesting that it may be magnetic fields rather than SN feedback that suppress ring star formation.

In this paper, we present results from magnetohydrodynamic (MHD) simulations of star-forming, magnetized nuclear rings. This work extends Paper I by considering magnetized gas inflows at the domain boundaries. To focus on the effects of magnetic fields on ring star formation, we fix the mass inflow rate and charac-

teristic ring radius (based on the imposed angular momentum of inflowing gas), while varying the magnetic field strength of the inflowing gas. By comparing the results from models with different field strengths, we quantify how magnetic fields affect dynamical evolution of nuclear rings and star formation therein.

In addition to allowing us to study effects of magnetization on star formation, our models are useful to explore how magnetic fields affect accretion in the central region of galaxies. In particular, our magnetized simulations show that gas accretes inward from the star-forming nuclear ring, which could potentially lead to formation of a circumnuclear disk (CND) near the galactic center. Based on the measured strength and pitch angle of magnetic fields in the nuclear ring of NGC 1097, Beck et al. (2005) suggested that magnetic stress can drive gas accretion from a ring to fuel an active galactic nucleus (AGN). Other proposed mechanisms for gas inflows near a galaxy center include bars-within-bars (Shlosman et al. 1989), nuclear spirals (Maciejewski 2004; Kim & Elmegreen 2017), and SN feedback (Wada 2004; Tress et al. 2020). Here we use direct numerical simulations to study gas accretion and its outcomes in the presence of magnetic fields and star formation feedback.

The remainder of this paper is organized as follows. In Section 2, we outline the equations that we solve, summarize the TIGRESS¹ numerical framework for the ISM and star formation physics, and describe our treatment of the boundary conditions for magnetized gas inflows. In Section 3, we present the overall time evolution of our models with a focus on star formation histories, and examine gas accretion toward the center driven by magnetic stresses. In Section 4, we present the temporal evolution of the magnetic field strength in the ring and explore the effects of magnetization on the ring star formation. Finally, we summarize and discuss our results in Section 5.

2. NUMERICAL METHODS

To numerically model the central kiloparsec region of a barred galaxy with high resolution, we adopt the semi-global numerical model introduced by Paper I. In this approach, our computational domain covers only the nuclear ring and its immediate vicinity, and bar-driven mass inflows are treated by boundary conditions. Nonlinear interactions between the bar and gas lead-

¹ TIGRESS is an acronym for “Three-phase Interstellar medium in Galaxies Resolving Evolution with Star formation and Supernova feedback”

Table 1. Model parameters

Model	R_{ring}	\dot{M}_{in}	β_{in}	$B_{\text{in},c}$	$B_{\text{in,avg}}$
(1)	(2)	(3)	(4)	(5)	(6)
	(pc)	($M_{\odot} \text{ yr}^{-1}$)		(μG)	(μG)
Binf	500	1.0	∞	0	0
B100	500	1.0	100	1.6	0.76
B30	500	1.0	30	3.0	1.4
B10	500	1.0	10	5.2	2.4

ing to the gas inflows are assumed to occur outside of the computational domain, and are not explicitly modeled. Instead, we control the mass inflow rate and angular momentum of the inflows using free parameters. In this section, we present the basic equations we solve (Section 2.1), summarize the TIGRESS framework for star formation and feedback (Section 2.2), and describe the inflow boundary conditions for magnetized gas (Section 2.3).

2.1. Governing Equations

Our computational domain is a Cartesian cube with side $L = 2048 \text{ pc}$ located at the galaxy center. The domain rotates at an angular frequency $\Omega_p = 36 \text{ km s}^{-1} \text{ kpc}^{-1} \hat{\mathbf{z}}$, corresponding to the adopted bar pattern speed². We include radiative heating and cooling of the ISM, gaseous self-gravity, and a fixed external gravitational potential responsible for the background rotation curve. The governing equations we solve are

$$\frac{\partial \rho}{\partial t} + \nabla \cdot (\rho \mathbf{v}) = 0, \quad (1)$$

$$\begin{aligned} \frac{\partial(\rho \mathbf{v})}{\partial t} + \nabla \cdot (\rho \mathbf{v} \mathbf{v} + P\mathbb{I} + \mathbb{T}) \\ = -2\rho\Omega_p \times \mathbf{v} - \rho\nabla\Phi_{\text{tot}}, \end{aligned} \quad (2)$$

$$\begin{aligned} \frac{\partial E}{\partial t} + \nabla \cdot [E\mathbf{v} + (P\mathbb{I} + \mathbb{T}) \cdot \mathbf{v}] \\ = -\rho \mathbf{v} \cdot \nabla \Phi_{\text{tot}} - \rho \mathcal{L}, \end{aligned} \quad (3)$$

$$\frac{\partial \mathbf{B}}{\partial t} = \nabla \times (\mathbf{v} \times \mathbf{B}), \quad (4)$$

² Even though we do not include a bar potential explicitly, it is advantageous to work in the rotating frame, since then the nozzles for inflow streams (see section 2.3) may be kept fixed in both space and time.

$$\nabla^2 \Phi_{\text{self}} = 4\pi G(\rho + \rho_{\text{sp}}). \quad (5)$$

Here, ρ and ρ_{sp} are respectively the volume density of gas and young star particles that form, \mathbf{v} is the gas velocity in the rotating frame, P is the gas pressure, \mathbb{I} is the identity matrix, $\mathbb{T} = B^2/(8\pi)\mathbb{I} - \mathbf{BB}/(4\pi)$ is the Maxwell stress tensor, $E = \rho v^2/2 + P/(\gamma - 1) + B^2/(8\pi)$ is the total energy density with adiabatic index $\gamma = 5/3$, $\Phi_{\text{tot}} = \Phi_{\text{self}} + \Phi_{\text{ext}} + \Phi_{\text{cen}}$ is the total gravitational potential, consisting of the self-gravitational potential Φ_{self} , the external gravitational potential Φ_{ext} , and the centrifugal potential $\Phi_{\text{cen}} = -\frac{1}{2}\Omega_p^2(x^2 + y^2)$, and $\rho\mathcal{L}$ is the net cooling rate per unit volume.

In our models, the external gravity $\Phi_{\text{ext}} = \Phi_{\text{BH}} + \Phi_b$ arises from a central supermassive black hole and a stellar bulge. We note that we do not include a nonaxisymmetric bar potential. The black hole is modeled by a Plummer potential

$$\Phi_{\text{BH}} = -\frac{GM_{\text{BH}}}{\sqrt{r^2 + r_{\text{BH}}^2}} \quad (6)$$

with the mass $M_{\text{BH}} = 1.4 \times 10^8 M_{\odot}$ and the softening length $r_{\text{BH}} = 20$ pc. For the stellar bulge, we take

$$\Phi_b = -\frac{4\pi G\rho_{b0}r_b^3}{r} \ln\left(\frac{r}{r_b} + \sqrt{1 + \frac{r^2}{r_b^2}}\right). \quad (7)$$

with the central density $\rho_{b0} = 50 M_{\odot} \text{pc}^{-3}$ and the scale radius $r_b = 250$ pc. The resulting rotation curve and the circular velocity at the ring position are similar to those of NGC 1097 as reported in Onishi et al. (2015).

The net cooling rate of gas per unit volume in Equation (3) is given by

$$\rho\mathcal{L} = n_{\text{H}}(n_{\text{H}}\Lambda - \Gamma_{\text{PE}} - \Gamma_{\text{CR}}), \quad (8)$$

where $n_{\text{H}} = \rho/(\mu_{\text{H}}m_{\text{H}})$ is the hydrogen number density with the mean molecular weight per hydrogen $\mu_{\text{H}} = 1.4271$ assuming the solar abundances. For the cooling function $\Lambda(T)$, we take the fitting formula of Koyama & Inutsuka (2002) (see Kim et al. 2008 for a typo-corrected version) for $T < 10^{4.2}\text{K}$, and the tabulated collisional ionization equilibrium cooling curve at solar metallicity of Sutherland & Dopita (1993) for $T > 10^{4.2}\text{K}$. The gas temperature T is related to density and pressure via an ideal equation of state $P = \rho k_{\text{B}}T/(\mu m_{\text{H}})$, with the mean molecular weight $\mu(T)$ varying with T from $\mu_{\text{ato}} = 1.295$ for neutral gas to $\mu_{\text{ion}} = 0.618$ for fully ionized gas (Kim & Ostriker 2017).

In Equation (8), Γ_{PE} represents an idealized model of the photoelectric heating rate by far-ultraviolet (FUV) radiation impinging on dust grains, and is given by

$$\Gamma_{\text{PE}} = \Gamma_{\text{PE},0} \left(\frac{\mu(T) - \mu_{\text{ion}}}{\mu_{\text{ato}} - \mu_{\text{ion}}} \right) \left(\frac{J_{\text{FUV}}}{J_{\text{FUV},0}} + 0.0024 \right), \quad (9)$$

where $\Gamma_{\text{PE},0} = 2 \times 10^{26} \text{erg s}^{-1}$ (Koyama & Inutsuka 2002) and $J_{\text{FUV},0} = 2.1 \times 10^4 \text{erg s}^{-1} \text{cm}^{-2} \text{sr}^{-1}$ (Draine 1978) are normalization factors based on the solar neighborhood conditions. The term in the first parentheses in Equation (9) reduces the photoelectric heating at high T (since realistically dust grains would sublimate), shutting this heating off completely in the fully ionized gas. The small factor in the last parentheses represents a minor contribution from the metagalactic far ultraviolet (FUV) background.

We use the same approximate method as in Paper I to calculate the mean FUV intensity J_{FUV} from young star particles in the simulations. For this, we first calculate the luminosity surface density Σ_{FUV} of all star particles younger than 40 Myr in the simulation domain³, and then apply an approximate model for dust attenuation, setting

$$J_{\text{FUV}} = \frac{\Sigma_{\text{FUV}}}{4\pi} \left(\frac{1 - E_2(\tau_{\perp}/2)}{\tau_{\perp}} \right) e^{-n_{\text{H}}/n_0}. \quad (10)$$

Here, E_2 is the second exponential integral, $\tau_{\perp} = \kappa_d \Sigma$ with $\kappa_d = 10^3 \text{cm}^{-2} \text{g}^{-1}$ is the vertical optical depth for the mean gas surface density Σ averaged over the entire domain, and the factor in parentheses represents the average attenuation factor for a uniform-density slab with a uniform source distribution. The exponential factor represents local shielding, with n_0 the density above which this shielding becomes significant. For the models presented in this paper, we take $n_0 = 50 \text{cm}^{-3}$, which yields a dependence of J_{FUV} on density comparable to that obtained by applying the adaptive ray-tracing method of Kim et al. (2017) (for details of this comparison see Paper I).

Inside dense regions where FUV radiation is heavily shielded, the heating is dominated by the CR ionization. The adopted heating rate Γ_{CR} in Equation (8) is given by

$$\Gamma_{\text{CR}} = q_{\text{CR}} \xi_{\text{CR}} \left(\frac{\mu(T) - \mu_{\text{ion}}}{\mu_{\text{ato}} - \mu_{\text{ion}}} \right), \quad (11)$$

where $q_{\text{CR}} = 10 \text{eV}$ is the energy yield per ionization (Glassgold et al. 2012, see also Gong et al. 2017) and ξ_{CR} denotes the CR ionization rate. The term inside the parentheses is again to shut off the CR heating in fully ionized gas. Assuming that ξ_{CR} is proportional to the SFR surface density Σ_{SFR} and is attenuated by a factor of Σ_0/Σ above a critical gas surface density $\Sigma_0 = 10.7 M_{\odot} \text{pc}^{-2}$ (Neufeld & Wolfire 2017), we set

$$\xi_{\text{CR}} = \xi_{\text{CR},0} \frac{\Sigma_{\text{SFR}}}{\Sigma_{\text{SFR},0}} \min \left\{ 1, \frac{\Sigma_0}{\Sigma} \right\}, \quad (12)$$

³ The FUV luminosity-to-mass ratio of the star particles depends on their age based on STARBURST99 model calculations.

where $\xi_{\text{CR},0} = 2 \times 10^{-16} \text{s}^{-1}$ is the CR ionization rate in the solar neighborhood (Indriolo et al. 2007; Neufeld & Wolfire 2017).

Equations (1) to (4) are discretized on a uniform mesh with 512^3 cells: the corresponding grid spacing is $\Delta x = 4 \text{ pc}$. We update the physical quantities using a version of the Athena MHD code (Stone et al. 2008), which employs the MUSCL-Hancock scheme with the constrained transport algorithm to preserve $\nabla \cdot \mathbf{B} = 0$ within machine precision (Stone & Gardiner 2009), and applies the first-order flux correction when needed (Lemaster & Stone 2009). We apply the Green’s function convolution method aided by a fast Fourier transform (e.g., Skinner & Ostriker 2015) to solve the Poisson equation (Equation 5) with the vacuum boundary condition, i.e., $\Phi_{\text{self}} \rightarrow 0$ at infinity.

2.2. Star Formation and Feedback

We handle star formation and feedback using the TIGRESS framework (Kim & Ostriker 2017, see also Paper I), which we briefly summarize here. We refer the reader to Kim & Ostriker (2017) for a more complete description.

We create a sink particle whenever the following three conditions are met simultaneously: (1) $\rho > \rho_{\text{LP}} = 8.86c_s^2/(\pi G \Delta x^2)$ with a local sound speed c_s , the threshold density based on the Larson-Penston collapse solution, (2) Φ_{self} is a local minimum⁴ and (3) the velocity is converging in all directions. A portion of the gas mass in the surrounding 27 cells is converted to the initial mass of a newly created sink particle. Sink particles are allowed to accrete mass and momentum from their surroundings and merge with nearby particles within $3\Delta x$ until the onset of the first SN explosion ($\sim 4 \text{ Myr}$). For orbits of sink particles, we solve their equations of motion

$$\ddot{\mathbf{x}} = -\nabla\Phi_{\text{tot}} - 2\boldsymbol{\Omega}_p \times \dot{\mathbf{x}}, \quad (13)$$

using the Boris algorithm that preserves the Jacobi integral very accurately (Boris 1970, see also the Appendix of Paper I).

Sink particles with age less than 40 Myr exert feedback in the form of the photoelectric heating (Equation (9)), CR heating (Equation (11)), and type II SN explosions. The method of energy and momentum injection for a given SN event depends on the density of the ambient medium. If the ambient density is low enough that the shell-formation radius is expected to be resolved, we regard the SN remnants as being in the Sedov-Taylor

phase and inject 72% of the SN energy $E_{\text{SN}} = 10^{51} \text{ erg}$ in the form of thermal energy and the remaining 28% in the form of kinetic energy. If the ambient density is too high for the adiabatic stage of evolution to be resolved, we assume that the SN remnant has already cooled to enter the snowplow phase and inject radial momentum $p_* = 2.8 \times 10^5 M_\odot \text{ km s}^{-1} (n_{\text{H}}/\text{cm}^{-3})^{-0.17}$ as calibrated from higher-resolution simulations (Kim & Ostriker 2015a). In both cases, each SN event returns the ejecta mass $M_{\text{ej}} = 10 M_\odot$ from a sink particle back to the ISM.

2.3. Magnetized Inflow Streams

Paper I introduced the semi-global framework that treats bar-driven mass inflows via imposed boundary conditions for hydrodynamic simulations. Here, we modify the boundary conditions slightly to handle magnetized inflows.

We inject gas streams into the computational domain through two circular nozzles with radius $\zeta_{\text{in}} = 112 \text{ pc}$ placed at the y -boundaries: the coordinates of the nozzle centers are $(x, y, z) = (\mp b_{\text{in}}, \pm L/2, 0)$, where $b_{\text{in}} = 512 \text{ pc}$ is the impact parameter of the inflows (see Figure 3 of Paper I, for schematic diagram). Here and hereafter, the upper and lower signs correspond to the upper and lower nozzles, respectively. We set the streaming velocity at the nozzles to

$$\mathbf{v}_{\text{in}} = \mp v_{\text{in}} (\sin \theta_{\text{in}} \hat{\mathbf{x}} + \cos \theta_{\text{in}} \hat{\mathbf{y}}), \quad (14)$$

where $\theta_{\text{in}} = 10^\circ$ is the inclination angle of the streams relative to the y -axis. The condition of the angular momentum conservation implies that the inflow speed v_{in} determines the location where the nuclear ring forms. By setting the specific angular momentum (in the inertial frame) of the inflows equal to $R_{\text{ring}} v_{\text{rot}}(R_{\text{ring}})$ with the circular velocity $v_{\text{rot}} \equiv (R d\Phi_{\text{ext}}/dR)^{1/2}$, we obtain

$$v_{\text{in}}(x, \pm L/2) = \frac{R_{\text{ring}} v_{\text{rot}}(R_{\text{ring}}) - R^2 \Omega_p}{|x \cos \theta_{\text{in}} \mp (L/2) \sin \theta_{\text{in}}|}. \quad (15)$$

We fix the ring radius to $R_{\text{ring}} = 500 \text{ pc}$ and use Equations (14) and (15) to find the corresponding inflow velocity inside the nozzles, which varies from 72 km s^{-1} to 115 km s^{-1} .

The density ρ_{in} of the streams sets the mass inflow rate as

$$\dot{M}_{\text{in}} = \iint \rho_{\text{in}} v_{\text{in}} \cos \theta_{\text{in}} dx dz, \quad (16)$$

where the integrations are performed over the two nozzles, i.e., $y = \pm L/2$ and $[(x \pm b_{\text{in}})^2 + z^2]^{1/2} < \zeta_{\text{in}}$. We fix the mass inflow rate to $1 M_\odot \text{ yr}^{-1}$ by taking $\rho_{\text{in}} = 0.138 M_\odot \text{ pc}^{-3}$, corresponding to $n_{\text{H}} = 3.9 \text{ cm}^{-3}$.

⁴ Φ_{ext} and Φ_{cen} vary very slowly in space and thus have negligible contribution to the gradients of Φ_{tot} .

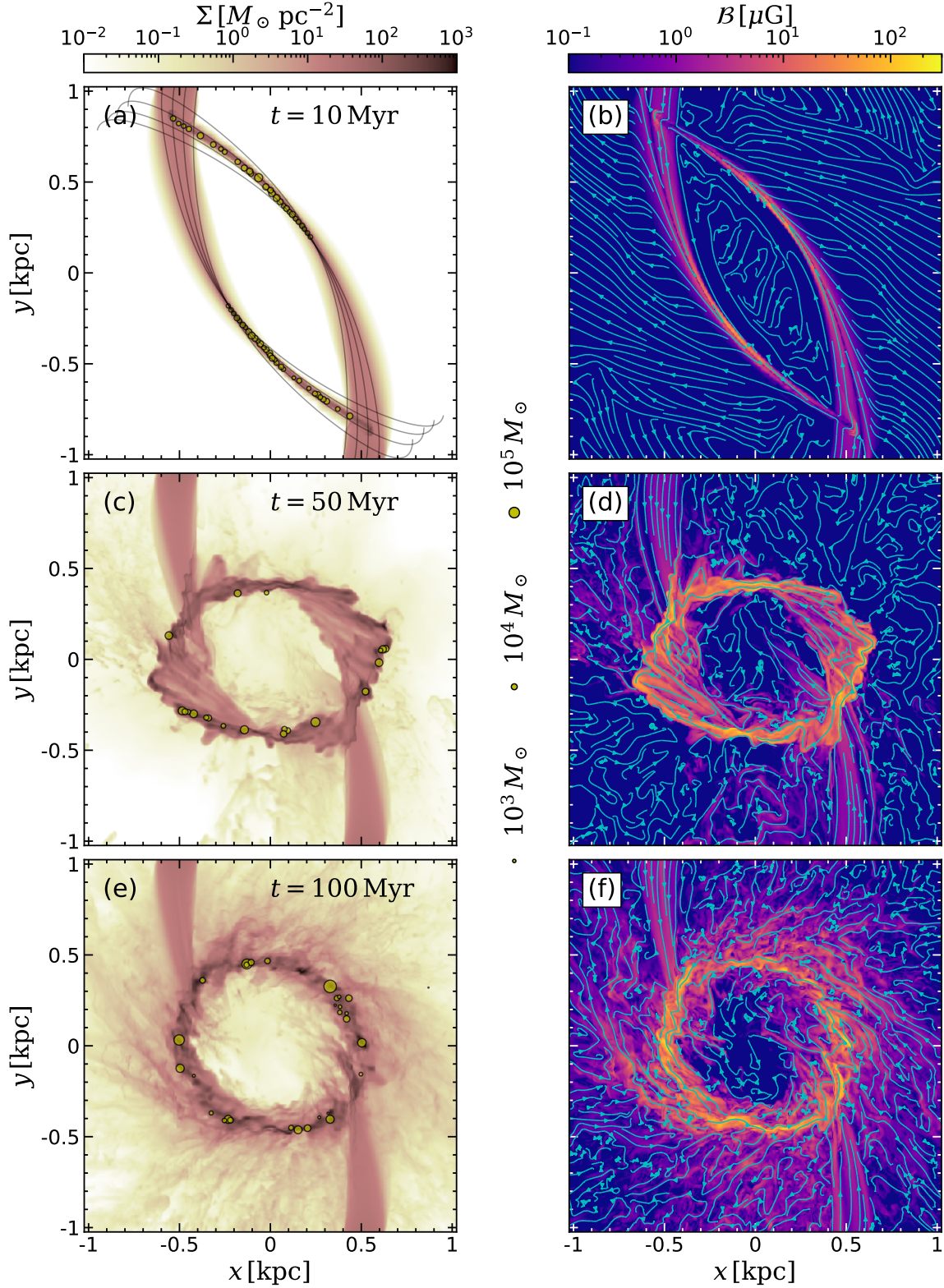


Figure 1. Face-on views of model B100 at $t = 10, 50, 100, 220, 250,$ and 285 Myr (the figure continues on the next page). The left column displays the gas surface density (color scale) and newly formed star particles with age $< 1 \text{ Myr}$ (circles). The right column plots streamlines of the projected magnetic fields $B_x = (\int \rho B_x dz) / (\int \rho dz)$ and $B_y = (\int \rho B_y dz) / (\int \rho dz)$, overlaid on maps of $B = (B_x^2 + B_y^2)^{1/2}$ (color scale). The black solid lines in the panel (a) are the ballistic trajectories that a test particle injected with \mathbf{v}_{in} would follow.

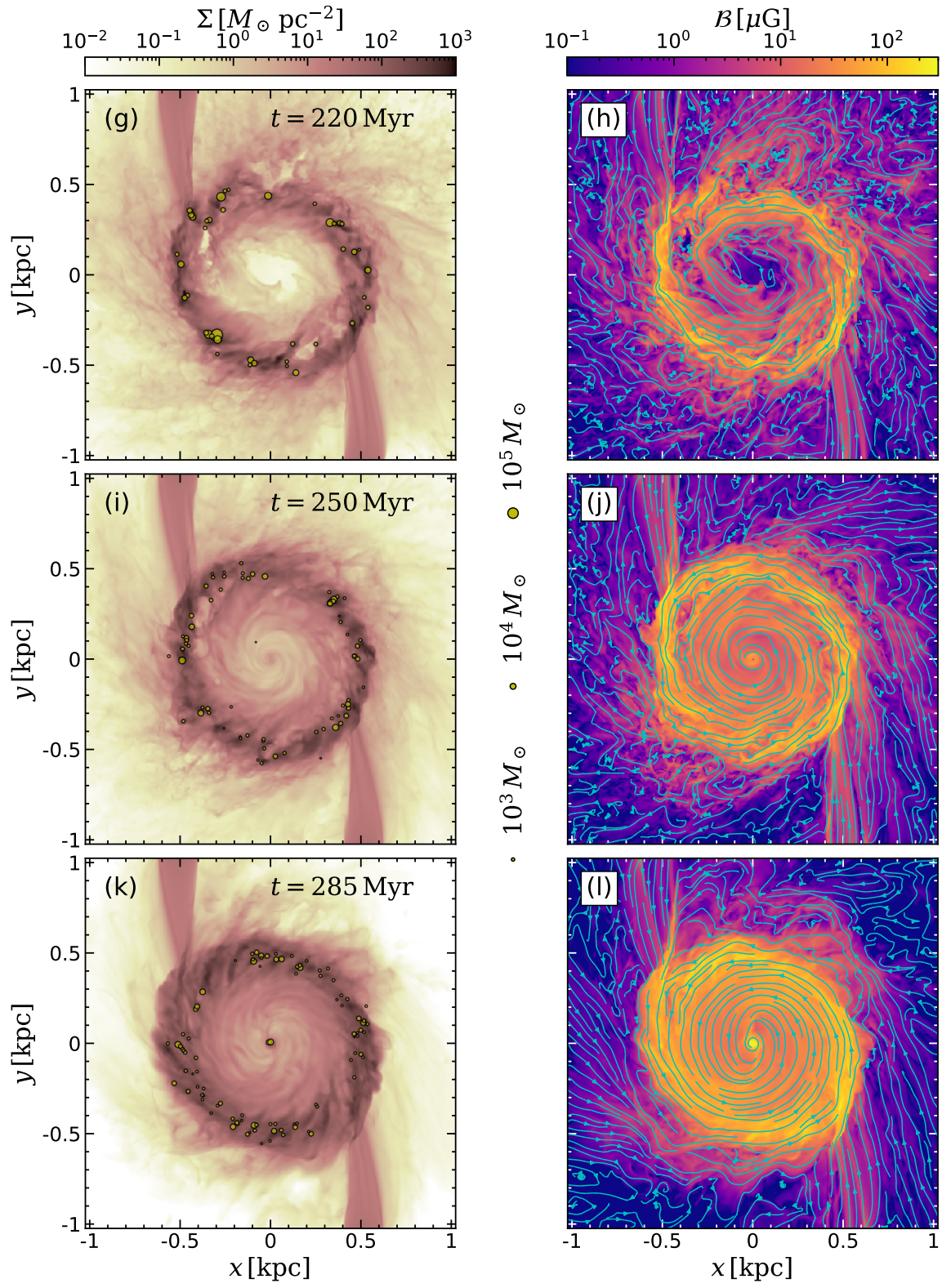


Figure 1. continued

The mean inflow speed in the nozzles amounts to $\bar{v}_{\text{in}} \equiv \dot{M}_{\text{in}} / (2\rho_{\text{in}}\pi\zeta_{\text{in}}^2 \cos\theta_{\text{in}}) = 91 \text{ km s}^{-1}$.

Radio polarization observations indicate that the magnetic fields are roughly parallel to dust lanes and point to the galactic center (Beck et al. 2005; Lopez-Rodriguez et al. 2021). Motivated by this, we take the magnetic fields inside the nozzles parallel to the inflow velocity as

$$\mathbf{B}_{\text{in}} = \frac{B_{\text{in}}}{v_{\text{in}}} \mathbf{v}_{\text{in}}, \quad (17)$$

with the amplitude

$$B_{\text{in}} = \left(\frac{8\pi P_{\text{in}}}{\beta_{\text{in}}} \right)^{1/2} \cos\left(\frac{\pi\zeta}{2\zeta_{\text{in}}} \right). \quad (18)$$

Here, $P_{\text{in}} = \rho_{\text{in}}k_{\text{B}}T_{\text{in}}/(\mu_{\text{H}}m_{\text{H}})$ is the thermal pressure of the inflowing gas with temperature $T_{\text{in}} = 2 \times 10^4 \text{ K}$, β_{in} is a plasma parameter measuring the ratio of thermal to magnetic pressure, and $\zeta = [(x \pm b_{\text{in}})^2 + z^2]^{1/2}$ is the distance from the nozzle center. The cosine term ensures that the fields vanish at the nozzle boundaries, preventing the gas just outside the nozzles from accidentally acquiring too large Alfvén speeds. In *Athena*, the velocity and magnetic fields are cell-centered and face-centered, respectively. Despite Equation (17), the mismatch in the evaluation points of \mathbf{B}_{in} and \mathbf{v}_{in} yields non-vanishing $\mathbf{v}_{\text{in}} \times \mathbf{B}_{\text{in}}$ at the innermost ghost zones at early time, as explained in Appendix A. This allows seed magnetic fields to leak into our computational domain through Equation (4), which are subsequently stretched by the inflows to become parallel to the streams, smoothly matching the boundary conditions (see Section 3.1).

We allow gas to freely escape from the simulation domain, but forbid inflows except through the nozzles. We accomplish this by setting the hydrodynamic variables in the ghost zones by extrapolating from the two adjacent active zones, while keeping the normal velocity to zero if the velocity is directed inward. The magnetic fields in the ghost zones are simply copied from the innermost active zones.

2.4. Models

We consider four models with $\beta_{\text{in}} = \infty, 100, 30,$ and 10 for the plasma beta parameter in the inflow. Table 1 summarizes the model parameters for all models. Column (1) lists the model names. Columns (2) and (3) give the ring radius and the mass inflow rate, respectively, which are the same for all models. Column (4) gives β_{in} . Column (5) and (6) give the magnetic field strength at the nozzle centers $B_{\text{in},c} = B_{\text{in}}(\zeta = 0)$ and the mean field strength inside the nozzles $B_{\text{in,avg}}$, respectively. Model B100 is our fiducial model which

has $\beta_{\text{in}} = 100$, $B_{\text{in},c} = 1.6 \mu\text{G}$, and $B_{\text{in,avg}} = 0.76 \mu\text{G}$. The simulation domain is initially filled with rarefied gas with density $n_{\text{H}} = 10^{-5} \exp[-|z|/(50 \text{ pc})] \text{ cm}^{-3}$ and temperature $T = 2 \times 10^4 \text{ K}$, and subsequent evolution is governed entirely by the inflowing streams.

3. EVOLUTION

In this section, we describe overall evolution of our fiducial model B100 in terms of the gas and magnetic field distribution and star formation. We also measure the accretion rates inside the ring and compare them with theoretical predictions.

3.1. Overall Evolution

Figure 1 plots snapshots of gas surface density together with young star particles as well as the projected magnetic field lines overlaid over the total field strength map in our fiducial model B100 at a few selected epochs. Figure 2 shows similar plots for models B100, B30, and B10 at a selected epoch for each model. Figure 3 plots evolution of the radial profiles of the azimuthally-averaged surface density for all models.

Early evolution of model B100 is qualitatively similar to that of the unmagnetized models presented in Paper I. There is an initial transient phase during which the inflows follow nearly ballistic orbits (Figure 1(a)), but within half an orbital time ($\sim 8 \text{ Myr}$), the streams from the opposite boundaries collide with each other, which drives strong shocks with a Mach number ~ 16 . The streams lose their orbital kinetic energy as they pass through the shocks multiple times, and form a nuclear ring with radius $R \sim R_{\text{ring}}$ at $t \sim 50 \text{ Myr}$ (corresponding to ~ 3 orbital times; see Figure 1(c)).

Still, the ring is elongated with the major axis precessing under the external gravitational potential. It takes another $\sim 50 \text{ Myr}$ for the ring to fully circularize (Figure 1(e,f)). The ring soon reaches a quasi-steady equilibrium where the FUV and CR heating balances the radiative cooling, the SN feedback balances the turbulent dissipation, and the thermal and turbulent pressures remain approximately constant. The resulting total mid-plane pressure matches the overlying weight in the ring. The gas mass in the ring also stays roughly constant as the net mass inflow rate balances the star formation rate. Star formation proceeds randomly throughout the whole of the ring. Although the resulting SN feedback disperses the gas and drives turbulence locally and temporarily, it never destroys the ring entirely nor quenches star formation completely (Section 3.2; see also Paper I).

As mentioned in Section 2.3 (and Appendix A), our boundary conditions introduce weak seed magnetic fields in the active domain, which are stretched along

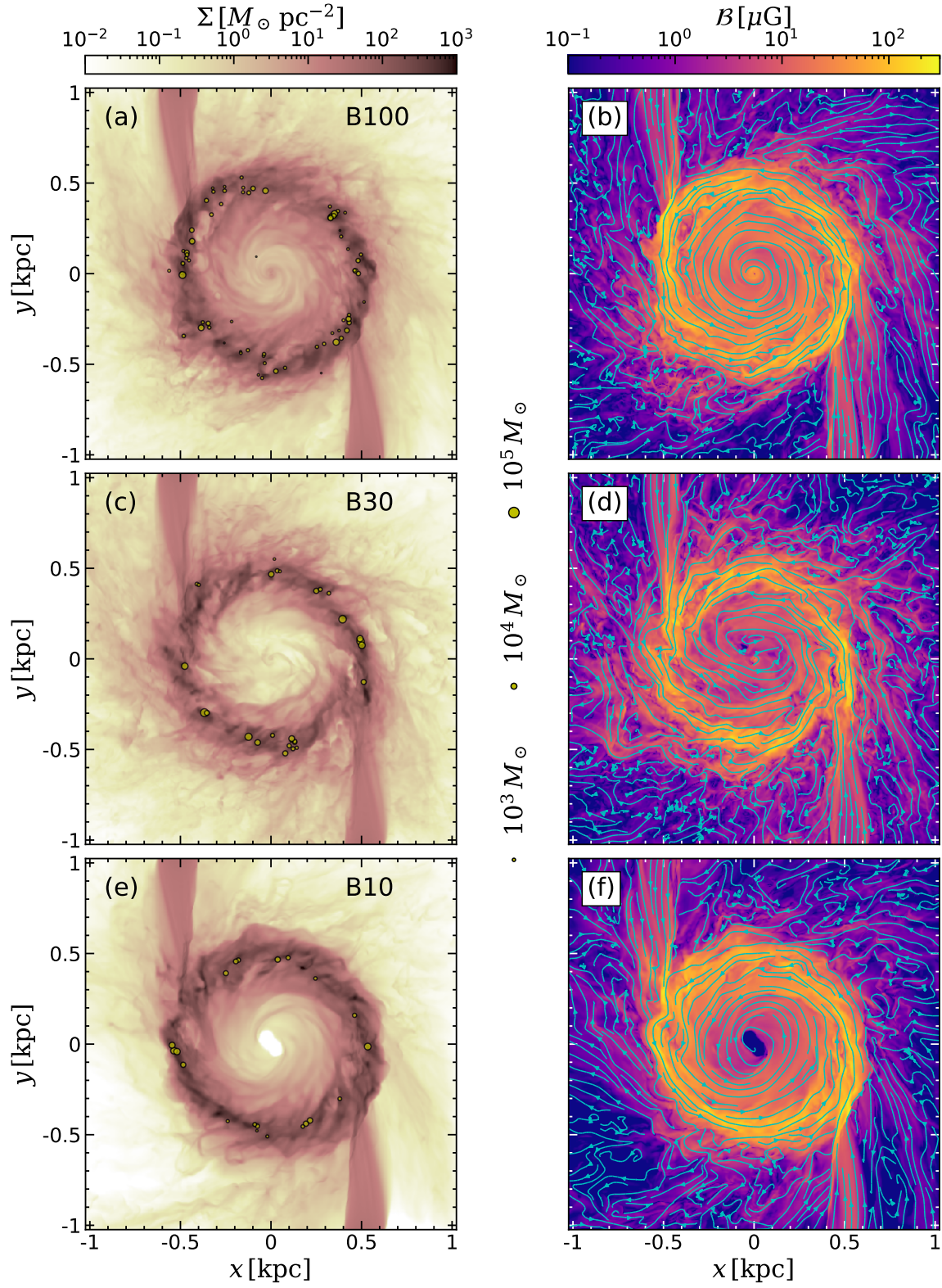


Figure 2. Similar to Figure 1, but for models B100, B30, and B10 at $t = 250, 130,$ and 130 Myr, respectively (from top to bottom).

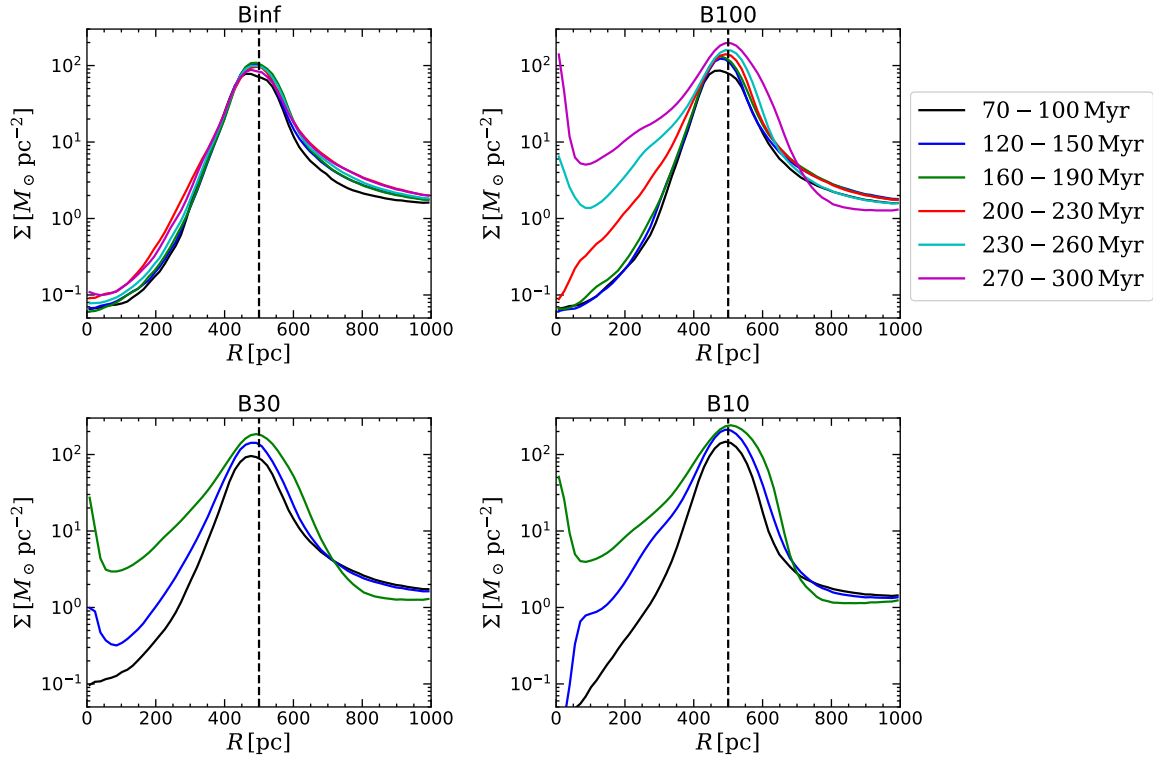


Figure 3. Evolution of the radial distribution of the azimuthally-averaged gas surface density for all models. Colors indicates the time interval for a temporal average. The vertical dashed lines mark the ring location $R_{\text{ring}} = 500$ pc.

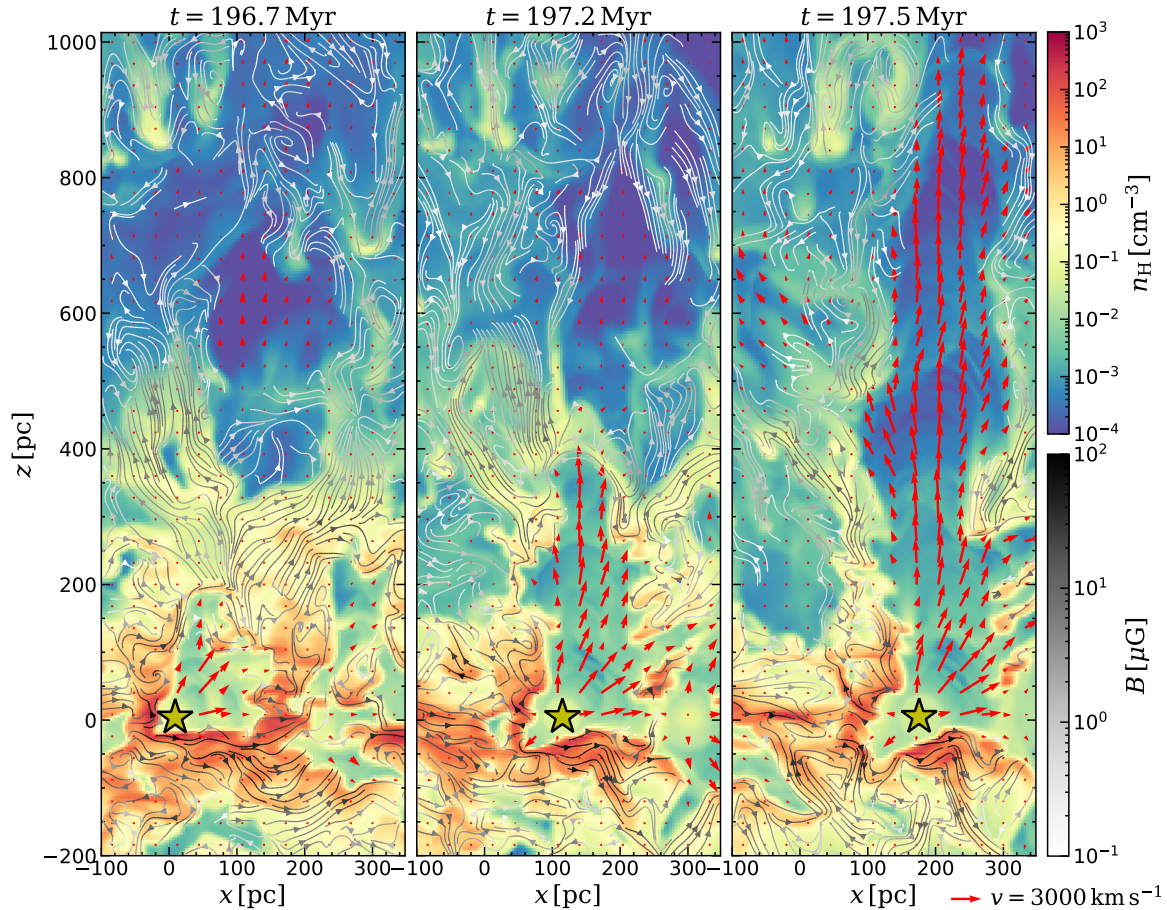


Figure 4. Superbubble breakout in the vertical direction. Each panel from left to right shows the density slice of model B100 at $y = -438$, -433 , and -419 pc, the y -position of a sink particle with mass $2 \times 10^6 M_{\odot}$ (denoted by the yellow star) at $t = 196.7$, 197.2 , and 197.5 Myr, respectively. The streamlines in grey represent the magnetic fields with the strength $B = (B_x^2 + B_y^2 + B_z^2)^{1/2} > 0.1 \mu\text{G}$. The red arrows are in-plane velocity vectors, (v_x, v_z) , with their lengths proportional to the speed $(v_x^2 + v_z^2)^{1/2}$. The expanding superbubble surrounding the star particle lifts the toroidal magnetic fields near the midplane to high-altitude regions to produce poloidal fields.

the streams by the inflowing gas. Except for initial ~ 10 Myr, magnetic fields in the streams remain well aligned with the inflow velocity and do not exhibit systematic growth in time, although they are perturbed intermittently by strong SN feedback from the ring. As the streams form a ring, magnetic fields become predominantly toroidal in the ring, with large fluctuations due to SN feedback. The magnetic fields in the ring become stronger and more regular with time (see Section 4.1), presumably due to both small- and large-scale dynamo driven by SN feedback and rotational shear inside the ring, the discussion of which we defer to Section 4.4.

Strong magnetic fields in the ring cause evolution of model B100 to deviate significantly from that of model Binf after $t \sim 200$ Myr in two ways. First, in contrast to model Binf where the surface density profile does not change much with time (Figure 3), an accretion flow develops in model B100 from the ring toward the center,

gradually filling the region inside the ring. The accreting gas piles up at the center, forming a CND with radius of ~ 50 pc. Second, strong magnetic fields and associated pressure make the SFR decrease with time in model B100 (see Section 4.2).

Figure 1(k) shows that much of the ring gas is concentrated in dense, trailing spiral segments with a pitch angle of $\lesssim 45^\circ$ and azimuthal spacing of ~ 100 – 150 pc. These spiral segments start to appear roughly at $t \sim 260$ – 270 Myr and keep being destroyed and regenerated thereafter. The quasi-regular spacing of these spiral segments suggests that they result from the magneto-Jeans instability (MJI) in which magnetic tension forces from bent field lines suppress the stabilizing effect of epicyclic motions (Elmegreen 1987; Kim & Ostriker 2001; Kim et al. 2002). Indeed, the corresponding dispersion relation (Equation 21 of Kim et al. 2002) for the parameters adopted from model B100 yields the most unstable wave-

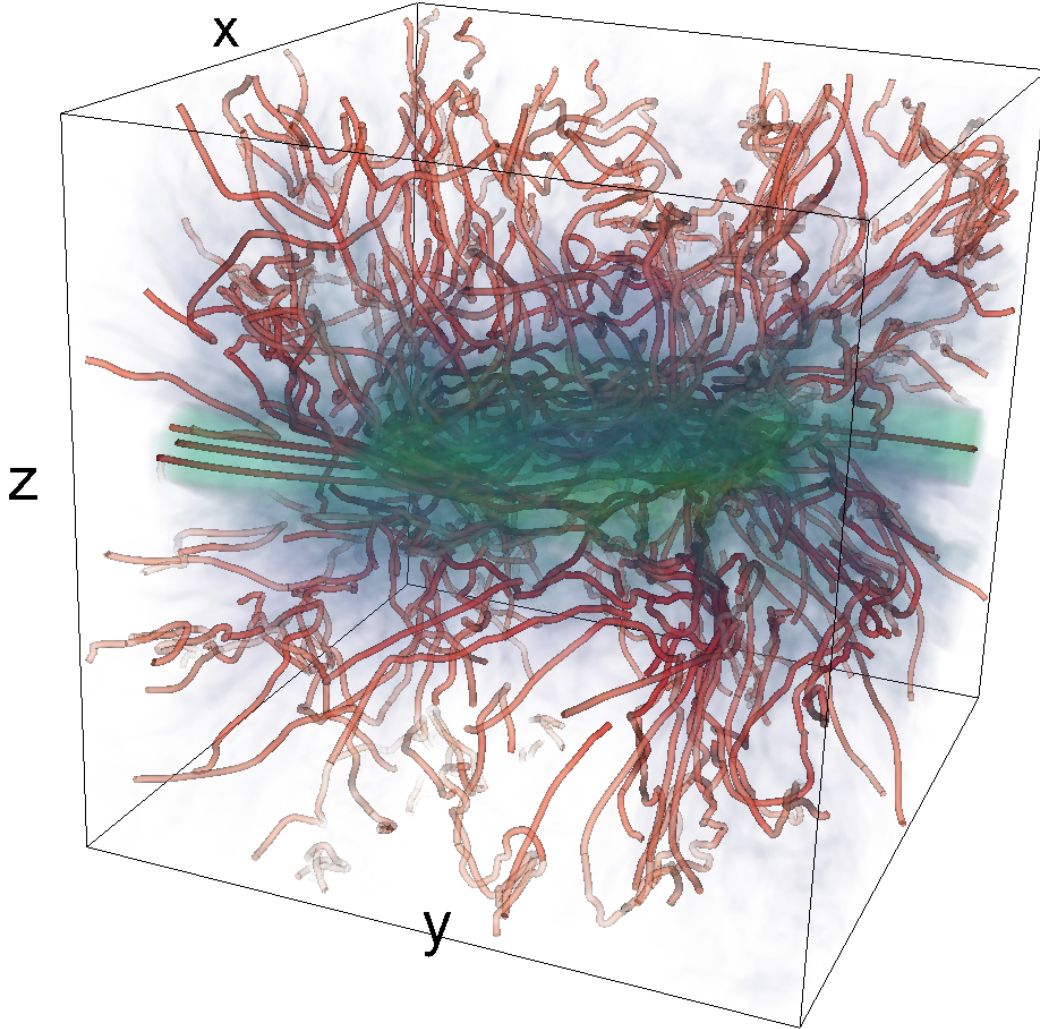


Figure 5. Perspective visualization of the three-dimensional magnetic field structure in model B100 at $t = 250$ Myr. The magnetic field lines are represented by red tubes, while the gas density is volume rendered in blue-green. Note that the magnetic fields are predominantly toroidal inside the nuclear ring because of the differential rotation, and poloidal in high- $|z|$ regions due to SN-driven outflows.

length of ~ 120 pc, entirely consistent with the numerical results. Due to the MJI, some spiral segments attain sufficient density to form stars. We note, however, that strong shear in the ring makes the MJI operate only temporarily, preventing runaway growth of spiral segments (see Section 4.2).

Figure 4 plots the spatial distribution of gas and magnetic fields in x - z slices through three consecutive positions of a moving star cluster with mass $2 \times 10^6 M_{\odot}$, marked by the star symbol in each panel. Repeated SN explosions create a superbubble around the cluster. The overpressurized bubble easily expands in the vertical direction where the gas density decreases, eventually breaking out and rapidly rising up with velocities exceeding 10^3 km s^{-1} . Magnetic field lines are lifted to high- $|z|$ regions and stretched by the flows of hot gas to

generate a poloidal component. Figure 5 plots a volumetric rendering of the three-dimensional magnetic field geometry and gas density, showing that the magnetic fields are predominantly toroidal in the ring and poloidal in the regions away from the midplane.

Evolution of models B10 and B30 is qualitatively similar to that of model B100 in the sense that the inflow streams collide to form a star-forming nuclear ring, and accretion flows develop from the ring toward the center when the magnetic stress becomes strong enough (see Section 3.3). However, the models with smaller β_{in} reach the evolutionary stage characterized by decreased SFR and an accretion flow from the ring toward the center at earlier time, compared to higher β_{in} models (see Figure 2). Figure 3 shows that unlike in model Binf, the rings in models B100, B30, and B10 expand

inward with time. The surface density interior to the magnetized rings increases with time due to the radial accretion flows, forming a CND characterized by the central upturn of the radial surface density profile at $R \lesssim 50$ pc. We note that we are unable to evolve the magnetized models for arbitrarily long time, because the Alfvén speed becomes too large in the low-density region above and below the magnetized CND, severely limiting the Courant-Friedrichs-Lewy timestep.

3.2. Star Formation History

We define the SFR, \dot{M}_{SF} , as the total mass of sink particles with age less than 10 Myr, divided by 10 Myr. Figure 6 plots the temporal histories of \dot{M}_{SF} , the total gas mass M_{gas} , the gas depletion time

$$t_{\text{dep}} = \frac{M_{\text{gas}}}{\dot{M}_{\text{SF}}}, \quad (19)$$

and the total magnetic energy E_{mag} inside the computational domain. For all models, there is initial transient behavior as the ring forms and star formation develops. After $t \sim 50$ Myr, the SFR becomes almost constant in model Binf, reaching a steady-state value $\dot{M}_{\text{SF}} \sim 0.8\text{--}0.9 M_{\odot} \text{yr}^{-1}$, with a factor of ~ 2 stochastic fluctuations due to turbulence driven by SN feedback, similar to the models presented in Paper I.

The star formation history of model B100 is very similar to that of model Binf until $t \sim 200$ Myr. After $t \sim 200$ Myr, however, strong magnetic fields in the ring of model B100 result in a reduced SFR. The evolution of the SFR in models B30 and B10 is qualitatively similar: it reaches a quasi-steady value at $t \sim 50\text{--}100$ Myr, which is lower by a factor of a few in the models with stronger magnetic fields (smaller β_{in}), and then starts to decline after $t \sim 120$ Myr. The secular trend of increasing M_{gas} evident in Figure 6(b) as well as increasing gas surface density in the ring (Figure 3) indicate that the decline of the SFR in magnetized models is not caused by the reduction in the gas mass or surface density. It is rather because a larger fraction of the ring gas becomes inert for star formation, as reflected in Figure 6(c) which shows that t_{dep} increases at late time. As the SFR drops below \dot{M}_{in} , the excess gas piles up in the ring and moves toward the center to form a CND.

Figure 6(d) shows that the magnetic energy in the computational domain exponentially increases with time, indicative of dynamo action. We note that the magnetic energy advected with the inflow streams is very small because $\mathbf{v} \parallel \mathbf{B}$ near the nozzles for most of the time, and therefore cannot account for the increase of E_{mag} (see Appendix B). We will present more detailed analysis on the growth of magnetic fields and their ef-

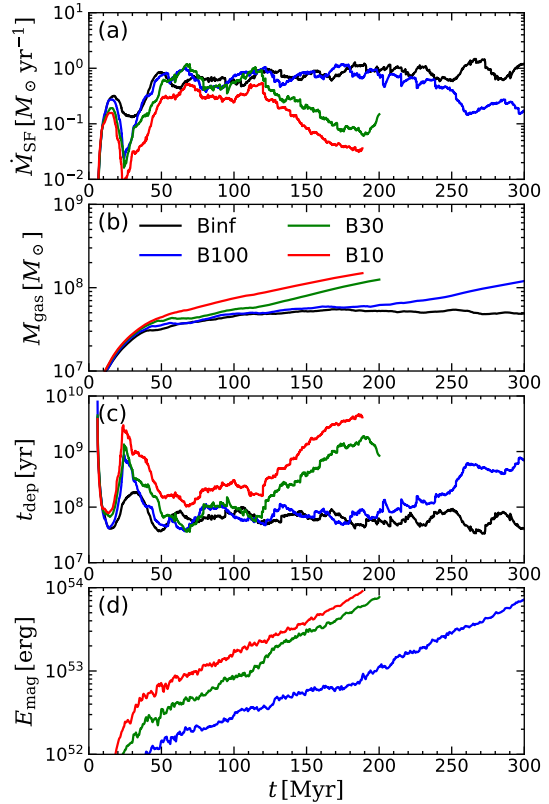


Figure 6. Temporal histories of (a) the SFR \dot{M}_{SF} , (b) the total gas mass M_{gas} , (c) the gas depletion time t_{dep} , and (d) the total magnetic energy inside the computational domain. The black, blue, green, and red lines correspond to models Binf, B100, B30, and B10, respectively.

fects on star formation, and discuss possible causes of the magnetic field amplification in Section 4.

3.3. Magnetically Driven Accretion Flow

Figures 1 and 3 show that all magnetized models develop an accretion flow from the ring toward the center. For rotating magnetized disks, Appendix C shows that the total mass accretion rate in a quasi-steady state can be written as

$$\dot{M}_{\text{acc}} \approx \dot{M}_{\text{M}} + \dot{M}_{\text{R}}, \quad (20)$$

where \dot{M}_{M} and \dot{M}_{R} are the mass accretion rates due to the Maxwell and Reynolds stresses, respectively, defined as

$$\dot{M}_{\text{M}} = 2\pi \left[\frac{\partial (Rv_{\text{circ}})}{\partial R} \right]^{-1} \frac{\partial \langle R^2 T_{R\phi} \rangle}{\partial R}, \quad (21a)$$

$$\dot{M}_{\text{R}} = 2\pi \left[\frac{\partial (Rv_{\text{circ}})}{\partial R} \right]^{-1} \frac{\partial \langle R^2 \rho u_R u_\phi \rangle}{\partial R}, \quad (21b)$$

where $v_{\text{circ}} = (\Omega - \Omega_p)R$ is the background circular velocity in the rotating frame and (u_R, u_ϕ) are the perturbation in the radial and azimuthal velocity. Figure 7 plots

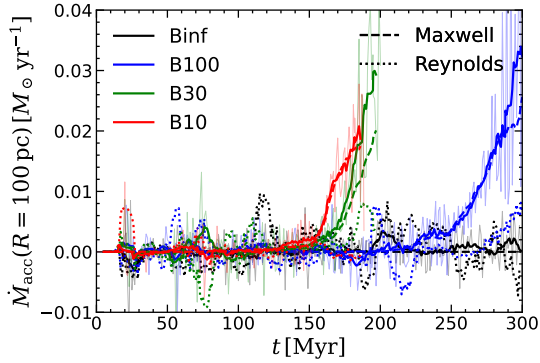


Figure 7. Temporal histories of the accretion rate \dot{M}_{acc} at $R = 100$ pc for models Binf (black), B100 (blue), B30 (green), and B10 (red). Thin and thick solid lines correspond to the instantaneous and time-averaged (using a 10 Myr window) values, respectively, directly measured from the simulations. Dashed and dotted lines are the predicted accretion rates due to the Maxwell and Reynolds stresses, using Equation (21) (averaged over a 10 Myr window), respectively. The increasing trend of \dot{M}_{acc} in magnetized models is well explained by the Maxwell stress.

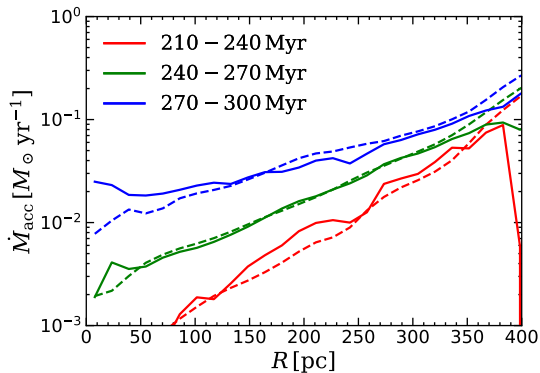


Figure 8. Radial profiles of the mass accretion rate at different epochs for model B100. Solid and dashed lines correspond to the measured accretion rate and predicted accretion rate due to the Maxwell stress, respectively.

the temporal histories of \dot{M}_{acc} measured at $R = 100$ pc for all models, in comparison with the predictions due to the Reynolds and Maxwell stresses. In model Binf, $\dot{M}_{\text{acc}} \sim 4 \times 10^{-4} M_{\odot} \text{ yr}^{-1}$ on average, showing that the mass accretion rate without magnetic fields remains small for all time. While the values of \dot{M}_{acc} in the magnetized models are also small at early times, they increase rapidly to reach $\dot{M}_{\text{acc}} \sim 0.02\text{--}0.03 M_{\odot} \text{ yr}^{-1}$ toward the end of the runs. The temporal changes of \dot{M}_{acc} are in good agreement with \dot{M}_{M} , indicating that magnetic tension is the major driver of mass accretion in our models.

Figure 8 plots the radial profiles of \dot{M}_{acc} averaged for a few selected time intervals for model B100, together

with \dot{M}_{M} . The accretion rate is not constant in radius but decreases toward the center, with a slope decreasing with time. This implies that mass is being deposited at all radii $< R_{\text{ring}}$, consistent with the radial density distributions shown in Figure 3. For $t = 270\text{--}300$ Myr, the accretion rate near the ring is $\sim 0.1 M_{\odot} \text{ yr}^{-1}$, i.e., one tenth of the bar-driven inflow rate, while it decreases to $0.02\text{--}0.03 M_{\odot} \text{ yr}^{-1}$ near the center. The radial dependence of the measured accretion rates is overall in good agreement with \dot{M}_{M} , indicating that the accretion flows are mediated mostly by the magnetic tension forces.

4. MAGNETIC FIELDS IN THE RING

In this section, we analyze evolution of the regular and turbulent magnetic fields in nuclear rings and explore their effects on the ring star formation. We also discuss vertical dynamical equilibrium in the presence of magnetic fields. Finally, we discuss our results in the context of dynamo theory.

4.1. Growth of Magnetic Fields

The magnetic fields inside the ring and its interior are close to axisymmetric (Figure 1), which motivates us to decompose the fields into a regular component $\bar{\mathbf{B}}$ and an irregular, turbulent component $\delta\mathbf{B}$ as

$$\mathbf{B}(R, \phi, z) = \bar{\mathbf{B}}(R, z) + \delta\mathbf{B}(R, \phi, z), \quad (22)$$

where the overbar denotes an azimuthal average

$$\bar{X}(R, z) \equiv \frac{1}{2\pi} \int_0^{2\pi} X d\phi, \quad (23)$$

for any physical quantity X . Note that $\delta\bar{\mathbf{B}} = 0$ by definition.

Figure 9 plots the spatial distributions of the azimuthally-averaged hydrogen number density \bar{n}_{H} , the strength of the regular component $|\bar{\mathbf{B}}| \equiv (\bar{B}_R^2 + \bar{B}_\phi^2 + \bar{B}_z^2)^{1/2}$, and the strength of the turbulent component $|\delta\bar{\mathbf{B}}|^{1/2} \equiv (\delta\bar{B}_R^2 + \delta\bar{B}_\phi^2 + \delta\bar{B}_z^2)^{1/2}$ in the R - z plane, for model B100 at $t = 200$ and 300 Myr. At $t = 200$ Myr, gas and magnetic fields are concentrated mostly in the nuclear ring delineated by the black circles centered at $(R, z) = (500, 0)$ pc with radius 200 pc, while the region outside the ring is filled with diffuse gas. At this time, magnetic fields are dominated by the turbulent component, especially outside the rings: the density-weighted (see below) mean strength of the regular and turbulent components are 8 and $22 \mu\text{G}$, respectively. The CND that begins to form near the center at $t \sim 250$ Myr due to magnetically-driven accretion from the ring is visible in the $t = 300$ Myr panels in the right column of Figure 9, as marked by the rectangles. The CND in our

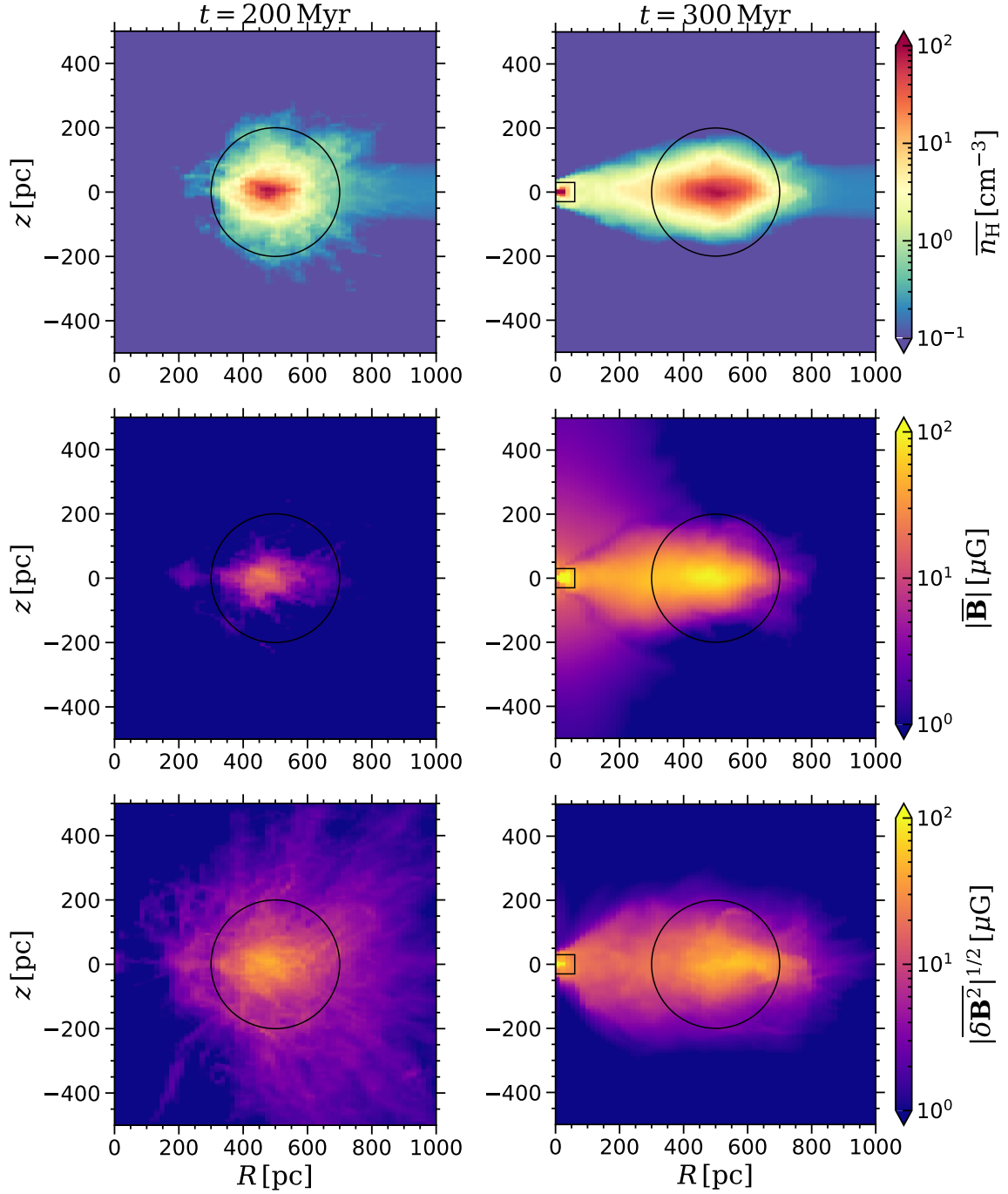


Figure 9. Spatial distributions from model B100 of the azimuthally-averaged hydrogen number density (top), and the strength of the regular (middle) and turbulent (bottom) components of the magnetic fields at $t = 200$ (left column) and 300 Myr (right column). The black circles centered at $(R, z) = (500, 0)$ pc with radius 200 pc outline the ring, while the rectangles near $R = 0$ in the right column mark a CND.

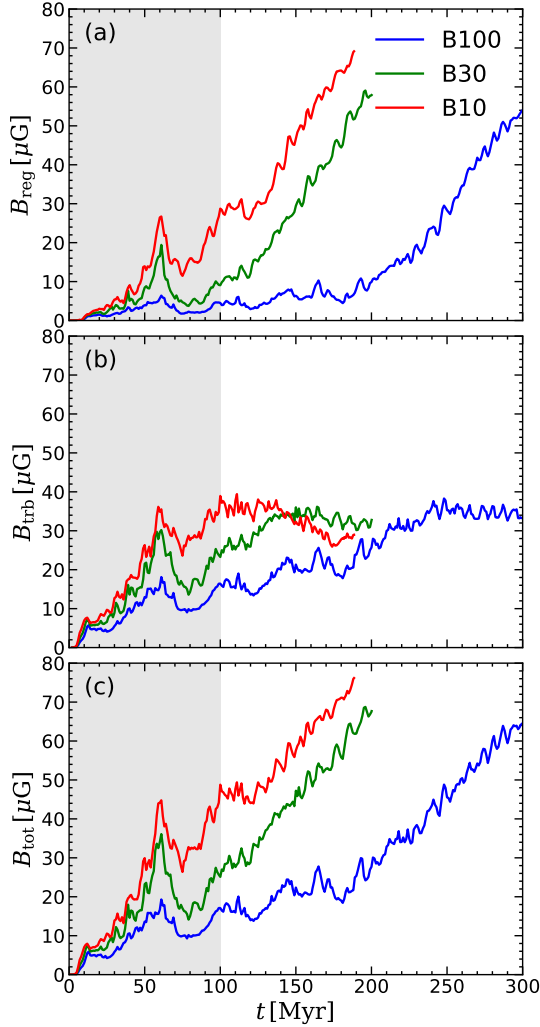


Figure 10. Temporal histories of the strength of the (a) regular, (b) turbulent, and (c) total magnetic field in the ring for models B100 (blue), B30 (green), and B10 (red). Magnetic fields are dominated by the turbulent component at early time, but become predominantly regular at late time. In the shaded regions at $t < 100$ Myr, the rings are not circular so that the decomposition of the magnetic fields into the regular and turbulent components is not meaningful.

models is denser and more strongly magnetized than the ring. At $t = 300$ Myr, the bottom two panels show that the regular magnetic field is stronger than the turbulent field in the ring.

To quantify the magnetic fields within the ring, we define the density-weighted average of the regular, turbulent, and total magnetic fields as

$$B_{\text{reg},j} \equiv \frac{\iint \bar{\rho} \overline{B_j} dRdz}{\iint \bar{\rho} dRdz}, \quad (24)$$

$$B_{\text{trb},j} \equiv \frac{\iint \bar{\rho} \overline{\delta B_j^2}^{1/2} dRdz}{\iint \bar{\rho} dRdz}, \quad (25)$$

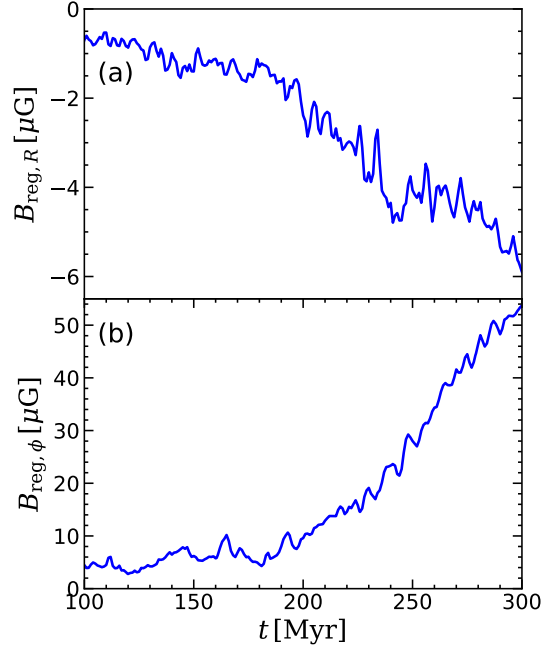


Figure 11. Temporal changes of the (a) radial and (b) azimuthal components of \mathbf{B}_{reg} for model B100. Note that $B_{\text{reg},R} < 0$, i.e., it points toward the center. The pitch angle $\theta_p \equiv -\tan^{-1}(B_{\text{reg},R}/B_{\text{reg},\phi})$ is roughly constant at $\theta_p \sim 12^\circ$ for $t = 100\text{--}240$ Myr and $\sim 6^\circ$ for $t = 270\text{--}300$ Myr.

$$B_{\text{tot},j} \equiv \frac{\iint \bar{\rho} \overline{B_j^2}^{1/2} dRdz}{\iint \bar{\rho} dRdz}, \quad (26)$$

where the integration is performed over the circular regions shown in Figure 9. Note that $\overline{B_j^2} = \overline{B_j}^2 + \overline{\delta B_j^2}$ by definition. Figure 10 plots the time evolution of $B_{\text{reg}} = |\mathbf{B}_{\text{reg}}|$, $B_{\text{trb}} = |\mathbf{B}_{\text{trb}}|$, and $B_{\text{tot}} = |\mathbf{B}_{\text{tot}}|$ for all models. We note that the ring is quite eccentric and undergoes damped oscillations of eccentricity before it enters a quasi-steady state at $t \sim 100$ Myr, in which case $\overline{\mathbf{B}}$ and $\delta\mathbf{B}$ do not properly represent the regular and turbulent components.⁵

The regular fields grow superlinearly in time (neglecting temporal fluctuations), reaching $B_{\text{reg}} \sim 50\text{--}70 \mu\text{G}$ at the end of the simulations. In contrast, the turbulent fields grow initially but saturate at $B_{\text{trb}} \sim 30\text{--}40 \mu\text{G}$. The total magnetic fields are initially dominated by the turbulent component, but are overtaken by the regular component at later time. The growth rate of the regular magnetic field at late time is largely insensitive to β_{in} , suggesting again that the field amplification is not due

⁵ During its eccentricity oscillations, the ring become almost circular at $t \sim 60$ Myr temporarily, producing the peak of B_{reg} , B_{trb} , and B_{tot} at that time.

to the advection of magnetic energy through the nozzles (see Appendix B). The magnetic fields grow earlier in models with smaller β_{in} because of the stronger seed fields. The growth of magnetic fields is most likely driven by SN feedback and rotational shear, which we will discuss in Section 4.4.

Figure 11 plots the temporal changes of the radial and azimuthal components of \mathbf{B}_{reg} for model B100 (the vertical component of \mathbf{B}_{reg} is negligible), showing that both components grow in time. The sign of the radial component is the opposite of the sign of the azimuthal field, implying a trailing spiral geometry (see Figure 1), consistent with observed large-scale magnetic fields in the nuclear ring of NGC 1097 (Beck et al. 1999, 2005; Lopez-Rodriguez et al. 2021). However, the pitch angle of the regular fields $\theta_p \equiv -\tan^{-1}(B_{\text{reg},R}/B_{\text{reg},\phi})$ is $\sim 6^\circ\text{--}12^\circ$, much smaller than $\theta_p \sim 40^\circ$ inferred from the observations; indeed, we would not expect that the field geometry probed by synchrotron emission would be directly comparable to the mass-weighted magnetic field we show here.

4.2. Effects of Magnetic Fields on Star Formation

It is well known that magnetic fields inhibit star formation by providing additional pressure and tension to resist gravitational collapse (e.g. Mestel & Spitzer 1956; McKee & Zweibel 1995; Hennebelle & Inutsuka 2019; Kim et al. 2021). To assess the dynamical importance of magnetic fields relative to thermal and turbulent pressures, we measure the sound speed c_s , vertical velocity dispersion σ_z , Alfvén speed associated with regular $v_{A,\text{reg}}$ and turbulent $v_{A,\text{trb}}$ magnetic fields of the cold–warm medium with $T < 2 \times 10^4$ K at the midplane as

$$c_s = \left(\frac{\iint_{z=-\Delta z}^{z=\Delta z} P\Theta \, dx dy dz}{\iint_{z=-\Delta z}^{z=\Delta z} \rho\Theta \, dx dy dz} \right)^{1/2}, \quad (27)$$

$$\sigma_z = \left(\frac{\iint_{z=-\Delta z}^{z=\Delta z} \rho v_z^2 \Theta \, dx dy dz}{\iint_{z=-\Delta z}^{z=\Delta z} \rho\Theta \, dx dy dz} \right)^{1/2}, \quad (28)$$

$$v_{A,\text{reg}} = \left(\frac{\iint_{z=-\Delta z}^{z=\Delta z} |\mathbf{B}|^2 \Theta \, dx dy dz}{4\pi \iint_{z=-\Delta z}^{z=\Delta z} \rho\Theta \, dx dy dz} \right)^{1/2}, \quad (29)$$

$$v_{A,\text{trb}} = \left(\frac{\iint_{z=-\Delta z}^{z=\Delta z} |\delta\mathbf{B}^2| \Theta \, dx dy dz}{4\pi \iint_{z=-\Delta z}^{z=\Delta z} \rho\Theta \, dx dy dz} \right)^{1/2}, \quad (30)$$

where $\Theta = 1$ for $T < 2 \times 10^4$ K and 0 otherwise (see Equation (22) and related text for definitions of $|\mathbf{B}|$ and $|\delta\mathbf{B}^2|$). Note that the integration in the horizontal directions is performed over the annular regions between

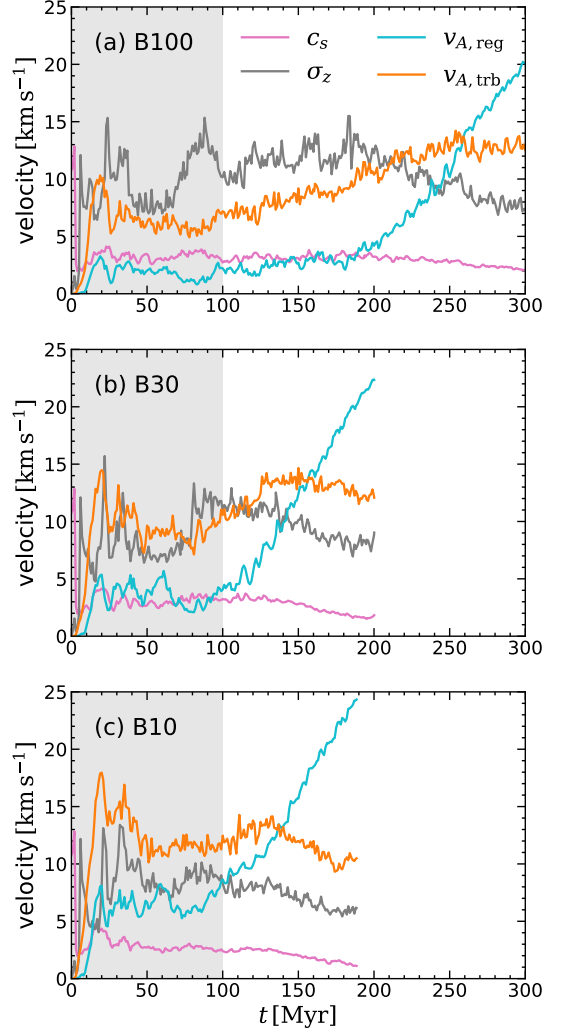


Figure 12. Temporal histories of the sound speed c_s (pink), the vertical velocity dispersion σ_z (gray), the Alfvén speed associated with the regular $v_{A,\text{reg}}$ (cyan) and turbulent $v_{A,\text{trb}}$ (orange) magnetic fields for models (a) B100, (b) B30, and (c) B10. The shaded region represents the epoch when the ring is not fully circularized.

$R_{\text{min}} = 300$ pc and $R_{\text{max}} = 700$ pc, i.e., the ring regions defined in Figure 9.

Figure 12 plots temporal histories of c_s , σ_z , $v_{A,\text{reg}}$, and $v_{A,\text{trb}}$ from the magnetized models, showing that $c_s \sim 3$ km s $^{-1}$ and $\sigma_z \sim 10$ km s $^{-1}$ with modest variations with time. The turbulent Alfvén speed saturates at a level where the turbulent magnetic energy is roughly comparable to the kinetic energy, with $v_{A,\text{trb}} \sim (1.5\text{--}1.8)\sigma_z$. The ratio of turbulent magnetic to turbulent kinetic energy found in previous simulations (Kim & Ostriker 2015b, 2017; Pakmor et al. 2017; Ostriker & Kim 2022) is in the range 0.2–0.5, similar or perhaps slightly below what we find here. In contrast, the regular Alfvén speed is initially constant, but exhibits secular

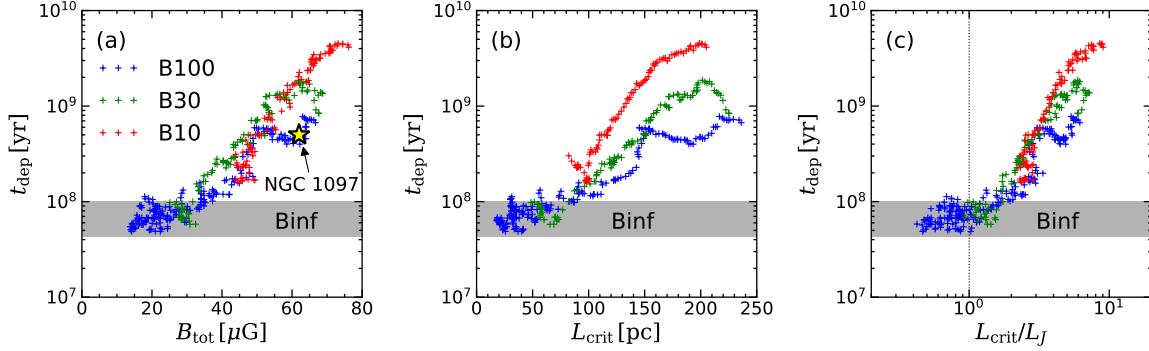


Figure 13. Gas depletion time as a function of (a) the total magnetic field strength in the ring, (b) the magnetic critical length $L_{\text{crit}} = G^{-1/2} R_{\text{ring}} (\Phi_M/M)$ (see text), and (c) a dimensionless ratio L_{crit}/L_J , where $L_J = [\pi c_s^2 / (G\rho)]^{1/2}$ is the Jeans length of the average cold–warm medium in the ring. Blue, green, and red symbols correspond to models B100, B30, and B10, respectively. The yellow star in the panel (a) marks the observed values for the nuclear ring of NGC 1097 (Tabatabaei et al. 2018; Prieto et al. 2019). The vertical dotted line in the panel (c) marks $L_{\text{crit}} = L_J$. The shaded region represents the range of the depletion time in model Binf for $t = 100\text{--}200$ Myr.

growth toward the end of each run, eventually overtaking $v_{A,\text{trb}}$ and reaching $v_{A,\text{reg}} > 20 \text{ km s}^{-1}$. The value of $v_{A,\text{reg}}$ begins to rise at ~ 200 Myr in model B100, and at ~ 120 Myr in models B30 and B10. Intriguingly, the period of rising $v_{A,\text{reg}}$ coincides with the period of rising t_{dep} for each model (see Figure 6).

Figure 13(a) plots the gas depletion time as a function of B_{tot} , showing that t_{dep} has a positive correlation with $B_{\text{tot}} \gtrsim 30 \mu\text{G}$, while it is almost independent of $B_{\text{tot}} \lesssim 30 \mu\text{G}$. When there are strong toroidal magnetic fields, a portion of a ring cannot collapse perpendicular to the magnetic fields unless it becomes massive enough by gathering mass along the field line. The minimum length that has to collapse along the field to become magnetically supercritical is given by

$$L_{\text{crit}} \equiv \frac{B}{2\pi G^{1/2} \rho} = \frac{R_{\text{ring}}}{G^{1/2}} \left(\frac{\Phi_M}{M} \right), \quad (31)$$

where Φ_M/M is the flux-to-mass ratio of the ring (Mestel & Spitzer 1956; Chen & Ostriker 2014). We calculate Φ_M/M inside the ring region defined in Figure 9 using $\Phi_M = \iint \bar{B}_\phi dR dz$. Figure 13(b) shows that t_{dep} has an overall positive correlation with L_{crit} , although different models have different t_{dep} at a given L_{crit} . Figure 13(c) plots t_{dep} against a dimensionless ratio L_{crit}/L_J , where $L_J \equiv [\pi c_s^2 / (G\rho)]^{1/2}$ is the Jeans length of the cold–warm medium in the ring⁶, showing that t_{dep} is approximately constant for $L_{\text{crit}}/L_J \lesssim 1$ but increases with $L_{\text{crit}}/L_J \gtrsim 1$. This is because as

⁶ For typical *ambient* cold–warm medium density, we take the volume-averaged density of the cold–warm medium between $R = 300$ and 700 pc at the midplane, with the density cut $n_{\text{H}} > 10 \text{ cm}^{-3}$ to exclude the warm, tenuous gas in the inflowing streams. For model B100 before $t \sim 200$ Myr, this is $\sim 100 \text{ cm}^{-3}$, a factor of ~ 4 smaller than the mass-weighted mean.

L_{crit} exceeds L_J , more and more Jeans-unstable clumps (smallest ones first) fail to ultimately collapse because they are magnetically subcritical. We note that at later time the MJI operates to gather material along the ring circumference. However, when L_{crit} exceeds the typical spacing ~ 100 pc between the spiral segments formed by the MJI, even the mass gathered by the MJI is not enough to overcome magnetic support. Overall, Figure 13 suggests that large-scale magnetic fields tend to suppress star formation in nuclear rings.

4.3. Vertical Dynamical Equilibrium

A framework developed to understand the co-regulation of galactic SFRs and ISM properties is the PRFM theory (Ostriker & Kim 2022; see also Ostriker et al. 2010; Ostriker & Shetty 2011). The theory assumes that the ISM in disk galaxies satisfies vertical dynamical equilibrium between the total midplane pressure and the weight of the overlying gas, and that it is star formation feedback that heats the gas and drives turbulence to maintain the required level of the midplane pressure. In this picture, the SFR is determined by the requirement for the feedback to yield the pressure needed for vertical dynamical equilibrium, which not only depends on the gas surface density but also on the local stellar density and the velocity dispersion (or gas scale height). Here we check if the vertical dynamical equilibrium holds in the magnetized nuclear ring, and assess the relative importance of the magnetic pressure to the other pressures.

We measure the thermal, turbulent, and magnetic pressures of the cold–warm medium at the midplane as

$$P_{\text{thm}} = \frac{\iiint_{z=-\Delta z}^{z=\Delta z} P \Theta dz dx dy}{\iiint_{z=-\Delta z}^{z=\Delta z} \Theta dz dx dy}, \quad (32)$$

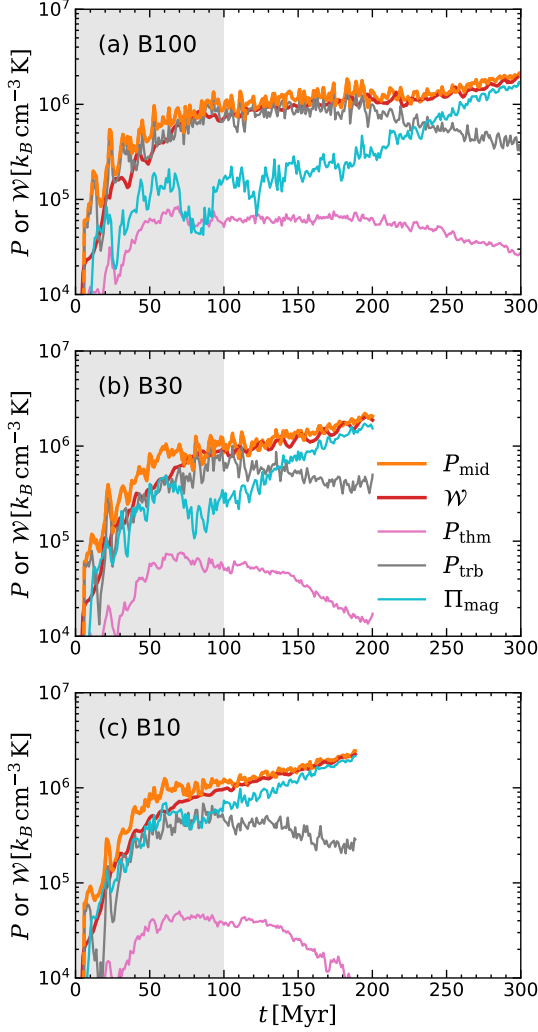


Figure 14. Temporal histories of the total midplane pressure (orange) and gas weight (red), as well as the thermal (pink), turbulent (gray), and magnetic (cyan) components of the midplane pressure, for models (a) B100, (b) B30, and (c) B10. After the ring enters the steady state at $t \sim 100$ Myr, $P_{\text{mid}} \approx \mathcal{W}$, indicating that the vertical dynamical equilibrium holds very well. The shaded region represents the epoch when the ring is not fully circularized.

$$P_{\text{trb}} = \frac{\iint \int_{z=-\Delta z}^{z=\Delta z} \rho v_z^2 \Theta dz dxdy}{\iint \int_{z=-\Delta z}^{z=\Delta z} \Theta dz dxdy}, \quad (33)$$

$$\Pi_{\text{mag}} = \frac{\iint \int_{z=-\Delta z}^{z=\Delta z} T_{zz} \Theta dz dxdy}{\iint \int_{z=-\Delta z}^{z=\Delta z} \Theta dz dxdy}, \quad (34)$$

where the integration in the horizontal directions is performed over the ring regions between $R_{\text{min}} = 300$ pc and $R_{\text{max}} = 700$ pc, and $\Theta = 1$ for $T < 2 \times 10^4$ K and 0 otherwise. Note that $T_{zz} = B^2/(8\pi) - B_z^2/(4\pi)$ so that Π_{mag} represents the total vertical magnetic stress, including

both magnetic pressure and tension terms (Boulares & Cox 1990; Piontek & Ostriker 2007; Kim & Ostriker 2015b). The weight of the ISM is given by

$$\mathcal{W} = \frac{1}{A_{\text{ring}}} \iiint_{z=0}^{z=L/2} \rho \frac{\partial \Phi_{\text{tot}}}{\partial z} dz dxdy, \quad (35)$$

where the horizontal integration is performed over the ring region as before, and $A_{\text{ring}} \equiv \pi(R_{\text{max}}^2 - R_{\text{min}}^2)$. It follows from Equation (2) that under quasi-steady equilibrium, $P_{\text{mid}} \equiv P_{\text{thm}} + P_{\text{trb}} + \Pi_{\text{mag}} \approx \mathcal{W}$ if the pressures at the horizontal and the upper boundaries of the cylindrical annulus are small compared to the midplane value.

Figure 14 plots P_{mid} and \mathcal{W} as well as the contributions of each pressure component for magnetized models, showing $P_{\text{mid}} \approx \mathcal{W}$ indeed holds well once the ring enters the quasi-steady state at $t \sim 100$ Myr⁷. While the midplane pressure is dominated by the turbulent component at early time, the magnetic pressure dominates after $t \sim 240$ Myr, ~ 140 Myr, and ~ 100 Myr for models B100, B30, and B10, respectively. As the ring becomes magnetically supported against the vertical gravity, the demand for the stellar feedback to replenish the thermal and turbulent pressures diminishes, causing the SFR to decline (Figure 6a), consistent with the PRFM theory.

4.4. Interpretation of the Field Growth

In our simulations, both regular and turbulent fields grow in strength with time, although the latter saturates at $\sim 35 \mu\text{G}$. The rapid growth and saturation of the turbulent magnetic fields are likely due to the SN-driven turbulence, which not only randomly stretches, twists, and folds the field lines to amplify them at small scales (Vainshtein & Zel'dovich 1972; Childress & Gilbert 1995), but also tangles the large-scale field lines to create fluctuating components. A number of simulations of the ISM where the turbulence is naturally driven by the SN feedback have demonstrated that the turbulent magnetic fields can be amplified out of very weak seed fields (e.g., Kim & Ostriker 2015b; Rieder & Teyssier 2016, 2017; Butsky et al. 2017; Pakmor et al. 2017; Gent et al. 2021). These studies have found that the growth rate of the turbulent dynamo is sensitive to the numerical resolution because the fastest growth occurs at the smallest resolvable scale, although the satu-

⁷ The average midplane pressure including hot ($T > 2 \times 10^4$ K) gas very well matches the weight for all time, even before $t \sim 100$ Myr; For $t < 100$ Myr, the average midplane pressure of the cold-warm medium is somewhat higher than the weight, indicating the hot gas pressure at those times is slightly smaller than that of the cold-warm medium.

ration amplitude is almost independent of the numerical resolution.

Compared to the small-scale dynamo, the large-scale dynamo responsible for the growth of ordered magnetic fields is still poorly understood. In part, the growth of B_{reg} in our simulations is presumably due to the strong differential rotation in the ring, which stretches radial fields into the azimuthal direction. However, the most naive version of the stretching effect is not evident in our simulations. For pure differential rotation $\mathbf{v} = \mathbf{v}_{\text{rot}} = R\Omega(R)\mathbf{e}_\phi$, it can be shown from Equations (4) and (23), and $\nabla \cdot \mathbf{B} = 0$ that

$$\frac{\partial \bar{B}_R}{\partial t} = 0, \quad (36a)$$

$$\frac{\partial \bar{B}_\phi}{\partial t} = -q\Omega \bar{B}_R, \quad (36b)$$

are exactly satisfied. Here, $q \equiv -d \ln \Omega / d \ln R$ is the rate of shear. In our simulations, $q = 0.87$ and $\Omega = 0.45 \text{ Myr}^{-1}$ at $R = R_{\text{ring}}$. Taking $\bar{B}_R = -1 \mu\text{G}$ as is true for $B_{\text{reg},R}$ at $t \sim 100 \text{ Myr}$ in model B100, Equation (36b) would imply a growth of \bar{B}_ϕ from zero to $40 \mu\text{G}$ in 100 Myr, vastly overestimating the true growth of $B_{\text{reg},\phi}$ shown in Figure 11. In addition, while Equation (36a) would predict $B_{\text{reg},R}$ to be constant in time, Figure 11 shows the magnitude of $B_{\text{reg},R}$ in fact grows in time.

The discrepancies with respect to the prediction of the simple shear model (Equation (36)) indicate that velocity components other than \mathbf{v}_{rot} play an important role in governing the growth of the regular magnetic fields in our simulations. Although a quantitative analysis of the large-scale dynamo that is responsible for growth of \mathbf{B}_{reg} is beyond the scope of this work, we provide a qualitative account of the mean field growth to motivate future work. One may write a general velocity field by

$$\mathbf{v} = \mathbf{v}_{\text{rot}} + \mathbf{v}_{\text{blk}} + \delta\mathbf{v}, \quad (37)$$

where $\mathbf{v}_{\text{blk}} \equiv \bar{\mathbf{v}} - \mathbf{v}_{\text{rot}}$ roughly corresponds to bulk motions of the fluid which deviate from circular rotation (e.g., bubble expansion and radial accretion), and $\delta\mathbf{v}$ is random turbulent motion. Here, $\bar{\mathbf{v}}$ and $\delta\mathbf{v}$ are similarly defined as Equation (22) such that $\overline{\delta\mathbf{v}} = 0$ by definition. Substituting Equation (37) into Equation (4) and applying the averaging of Equation (23), one obtains

$$\frac{\partial \bar{\mathbf{B}}}{\partial t} = -q\Omega \bar{B}_R \mathbf{e}_\phi + \nabla \times (\mathbf{v}_{\text{blk}} \times \bar{\mathbf{B}}) + \nabla \times (\overline{\delta\mathbf{v} \times \delta\mathbf{B}}). \quad (38)$$

In the mean-field dynamo theory for rotating systems, it is thought that the last term in Equation (38) captures the so called α effect in which the Coriolis force yields

systematic twists in the field lines to produce large-scale magnetic fields, as envisaged by Parker (1955), as well as turbulent diffusion of the mean magnetic fields (Brandenburg & Subramanian 2005). For example, by assuming weak Lorentz force and isotropic turbulence, the first-order smoothing approximation yields $\nabla \times (\overline{\delta\mathbf{v} \times \delta\mathbf{B}}) = \alpha \nabla \times \bar{\mathbf{B}} + \eta_t \nabla^2 \bar{\mathbf{B}}$, with the transport coefficients $\alpha \approx -(\tau_{\text{cor}}/3) \overline{\delta\mathbf{v} \cdot (\nabla \times \delta\mathbf{v})}$ and $\eta_t \approx (\tau_{\text{cor}}/3) \overline{\delta\mathbf{v}^2}$, where τ_{cor} is the correlation time of turbulence (Brandenburg & Subramanian 2005). If $B_{\text{reg},\phi}$ has a single sign and decreases in magnitude away from the midplane, as is true in our simulations, the radial component of $\nabla \times \bar{\mathbf{B}}$ will change sign across the midplane. Expansion of bubbles centered on the midplane in combination with the Coriolis force will tend to produce a kinetic helicity $\overline{\delta\mathbf{v} \cdot (\nabla \times \delta\mathbf{v})}$ that changes sign across the midplane (Ruzmaikin et al. 1988), and indeed we find this sign change when we measure kinetic helicity in our simulations. Thus, we can qualitatively understand the growth of $B_{\text{reg},R}$ as due to the combined effect of the midplane change in sign of α with the midplane change in sign of $(\nabla \times \bar{\mathbf{B}})_R$, to make the last term in Equation (38) keep the same sign across the midplane.

As discussed above, the presence of nonzero \bar{B}_R will tend to produce growth of \bar{B}_ϕ , as expressed by the first term proportional to Ω on the right-hand side of Equation (38). The combination of the two effects discussed above on mean field growth is often referred to as an “ α - Ω ” dynamo. The turbulent diffusion term $\eta_t \nabla^2 \bar{\mathbf{B}}$ will, however, tend to suppress growth of the mean field. Also, the second term on the right hand side of Equation (38) could in the case of our simulations represent advection of mean magnetic fields out of the ring due to the radial accretion flow, and/or dilution due to the expansion of SN remnants. Together with the turbulent diffusion, these bulk flows may account for the reduction in field growth compared to a pure α - Ω dynamo. We note that the regular magnetic fields grow faster when σ_z starts to decline (see Figures 11 and 12(a)), which is presumably due to the reduction of η_t with decreasing velocity dispersion (Gressel et al. 2008).

One important aspect of the α effect is that while it creates large-scale magnetic helicity associated with the poloidal loops, it does so at the expense of a small-scale magnetic helicity of an opposite sign, which is associated with the internal twist of the poloidal loops (see Blackman & Brandenburg 2003, for a visual illustration), in a way that satisfies magnetic helicity conservation. As small scale magnetic helicity (or “twists”) accumulates over time, the magnetic tension resists bending and twisting of the field lines to quench the α effect, potentially limiting the growth of regular magnetic

fields (see Section 9 of Brandenburg & Subramanian 2005). Shukurov et al. (2006) showed that galactic fountain flows can transport the small-scale helicity out of the disk in vertical direction, maintaining the dynamo against the back-reaction from the Lorentz force. In our simulations, clustered SN explosions are powerful enough to drive outflows that drag magnetic fields away from the midplane and to leave the computational domain (see Figure 4; see also Figure 8 of Paper I). Even when vertical outflows become weak as the growing magnetic fields suppress the SFR, the radial accretion flows may still be able to transport helicity out of the ring.

4.5. Resolution Dependence

To see how our results depend on numerical resolution, we rerun our fiducial model B100 at lower resolution, using 256^3 cells corresponding to $\Delta x = 8$ pc. Figure 15(a) compares the temporal evolution of the field strength between the 512^3 and 256^3 runs. Evidently, growth of the turbulent field B_{trb} is initially higher for the higher-resolution model, and the super-linear growth stage for the regular field B_{reg} also occurs earlier in time for the higher-resolution model. The initially faster growth of B_{trb} is presumably because the growth rate of the small-scale turbulent dynamo is inversely proportional to the eddy turnover time at the grid scale, as noted by Rieder & Teyssier (2016). The stronger turbulent fields at earlier time in the 512^3 run also presumably lead to earlier superlinear growth of B_{reg} . We note that the growth rate of B_{reg} at the time when B_{trb} saturates is similar in both models. The saturated field strength of B_{trb} is similar in both models (see also Figure 16 and related discussion of saturation).

Because magnetic field growth is delayed in the low-resolution model, other characteristic evolutionary effects affected by magnetic fields (see Section 3.1) also occur later in time. For example, Figure 15(b) and (c) show that the mass accretion rate and depletion time start to increase at $t \sim 200$ Myr and ~ 400 Myr in the 512^3 and 256^3 runs, respectively, corresponding to the start of the super-linear growth of B_{reg} . We note that even though the mass accretion rate at a given time depends on numerical resolution, it is entirely consistent with the predicted accretion rate from the instantaneous Maxwell stress.

5. SUMMARY AND DISCUSSION

5.1. Summary

Nuclear rings at the centers of barred galaxies are active in star formation (Mazzuca et al. 2008; Ma et al. 2018) and threaded by magnetic fields with a mean strength of ~ 50 – $100 \mu\text{G}$ (Beck et al. 2005; Yang et al.

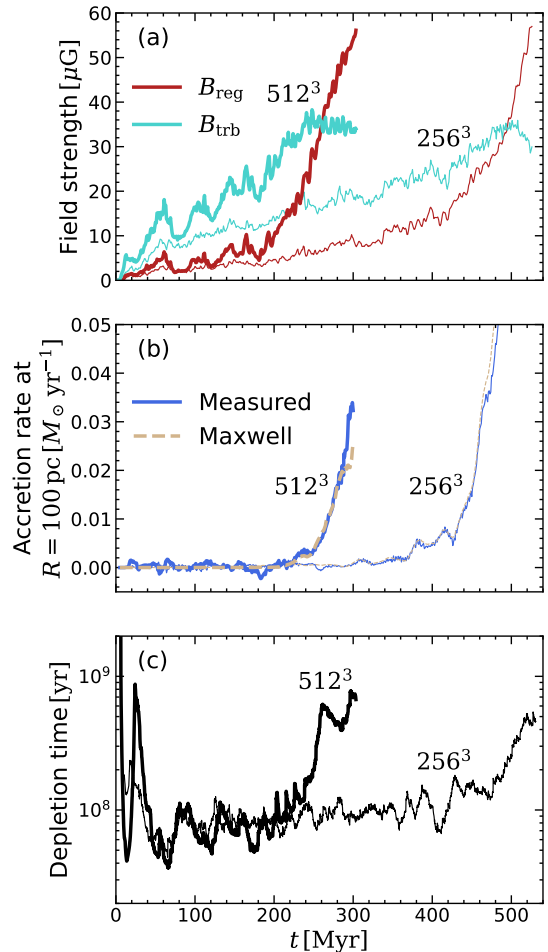


Figure 15. Resolution study. We compare the 512^3 ($\Delta x = 4$ pc; thick) and 256^3 ($\Delta x = 8$ pc; thin) runs with $\beta_{\text{in}} = 100$ for evolution of (a) the regular (brown) and turbulent (cyan) magnetic field strengths, (b) the measured (\dot{M}_{acc} ; blue solid) and predicted (\dot{M}_{M} ; gold dashed) mass accretion rates at $R = 100$ pc, and (c) the depletion time t_{dep} .

2022). To study how magnetic fields affect star formation in nuclear rings, we run MHD simulations of galactic centers. We employ the semi-global models of Paper I, in which magnetized gas streams from two nozzles at the boundaries supply gas and magnetic fields, mimicking bar-driven gas inflows along dust lanes. We adopt the modified TIGRESS framework (Kim & Ostriker 2017) to model star formation and related FUV and SN feedback, as well as the shielding of FUV radiation and CR heating in dense environments. We fix the mass inflow rate to $\dot{M}_{\text{in}} = 1 M_{\odot} \text{ yr}^{-1}$ and the ring size to $R_{\text{ring}} = 500$ pc, while varying the plasma parameter $\beta_{\text{in}} = 10, 30, 100$ to adjust the average field strength within the gas streams to $B_{\text{in,avg}} = 2.4 \mu\text{G}$, $1.4 \mu\text{G}$, and $0.76 \mu\text{G}$. We also run a hydrodynamic model with unmagnetized streams for comparison. The magnetic

fields in the streams are set parallel to the inflow velocity, motivated by observations (Beck et al. 2005; Lopez-Rodriguez et al. 2021).

The main results of this work can be summarized as follows:

1. *Overall Evolution:* The two gas streams injected from the domain boundaries at the opposite sides collide with each other after about half an orbital time, dissipating their orbital kinetic energy via shocks. As the gas orbits gradually circularize, a well-defined nuclear ring forms at the radius where the specific angular momentum of the inflowing gas matches that of the circular orbit. At about $t \sim 100$ Myr, the nuclear ring reaches a quasi-steady state in which the shape, SFR, and gas mass become approximately constant with time. Stars form randomly across the whole circumference of the ring, and the associated feedback renders the ring turbulent. When the magnetic fields in the ring become strong enough they reduce the ring SFR. At the same time, strong magnetic torques lead to accretion flows from the ring to the galaxy center (Figures 1 and 3), where a circumnuclear disk grows. Due to the action of MJI combined with strong shear, at late stages the ring forms transient trailing spiral segments, some of which undergo star formation.
2. *Magnetic Fields and Their Growth:* Magnetic fields in the ring can be separated into a regular and a turbulent component, where the former is defined via azimuthal averaging and the latter is the azimuthally fluctuating residual. The turbulent component grows in strength over time and saturates at $\sim 30\text{--}40 \mu\text{G}$ independent of β_{in} , likely due to the SN driven turbulent dynamo. In contrast, the regular component does not saturate but keeps growing with time, reaching $50\text{--}70 \mu\text{G}$ at the end of the runs (Figure 10). While the turbulent fields are approximately isotropic, the regular fields are dominated by the azimuthal component with a pitch angle of $\theta_p \sim 6^\circ\text{--}12^\circ$. The overall field direction is mostly toroidal near the midplane, but expansion of superbubbles created by clustered SNe drag the toroidal fields to produce poloidal fields in high-altitude regions (Figures 4 and 5).
3. *Magnetically Driven Accretion:* All our magnetized models develop accretion flows that slowly fill the region interior to the ring and eventually form a CND with radius $\lesssim 50$ pc at the center. This is in stark contrast to the unmagnetized model

where the region interior to the ring is always filled with hot, rarefied gas. The gas accretion rates measured in the simulations are consistent with the theoretical quasi-steady rates due to the Maxwell stress, indicating that the radial accretion is driven by magnetic tension. The measured accretion rate depends on the galactocentric radius and reaches $\sim (0.02\text{--}0.1) M_\odot \text{yr}^{-1}$ at late time (Figures 7 and 8).

4. *Effects of Magnetic Fields on Star Formation:* When strong magnetic fields develop in the ring, they suppress star formation therein. Consequently, the gas depletion time t_{dep} in the rings increases with the total field strength. In particular, strong regular azimuthal magnetic fields in the ring limit the radial and vertical compression that lead to collapse, unless the ring undergoes sufficient azimuthal contraction that could gather material along the field lines (Figure 13). The ring maintains vertical dynamical equilibrium instantaneously, meaning that the weight of the ISM is balanced by the midplane total pressure (Figure 14). While the magnetic pressure is negligible in the vertical force balance at early time, it becomes dominant at late times ($t \gtrsim 240$ Myr in model B100). This late-time strong magnetic support, which is mostly from the regular (non-turbulent) component of the magnetic fields, reduces the demand for SN feedback to replenish the thermal and turbulent pressures, thereby indirectly lowers the SFR, consistent with the PRFM theory of Ostriker & Kim (2022).

5.2. Discussion

Infrared polarization observations indicate that Galactic magnetic fields are preferentially toroidal near the CMZ and poloidal in the regions with Galactic latitudes $|b| > 0.4^\circ$ (Nishiyama et al. 2010). This toroidal-to-poloidal transition of the Galactic magnetic fields is consistent with our numerical results that expanding superbubbles drag the toroidal fields in the rings to produce poloidal magnetic fields in high-altitude regions (Figures 4 and 5). The poloidal magnetic walls of venting superbubbles are likely illuminated by relativistic particles accelerated in-situ at SN shocks, potentially creating some nonthermal radio filaments, such as Radio Arc and Sgr C filaments, found near radio bubbles (e.g., Heywood et al. 2022). For filaments without any evident source, Barkov & Lyutikov (2019) proposed that transiting pulsar wind nebulae may inject relativistic particles to make the background poloidal magnetic fields visible locally. Alternatively, Sofue (2023) proposed that the

filaments represent projected wavefronts of fast MHD waves launched from SNe exploding in the ring, which locally compress the existing magnetic fields. The results of our simulations suggest that the background volume-filling magnetic fields necessary in both scenarios can be produced by superbubbles breaking out of the ring.

The results of our simulations show that the magnetic torque produces significant inflows of gas from a nuclear ring toward the center, forming a CND. The mass accretion rate depends both on time and radius such that for model B100 at $t = 300$ Myr, $\dot{M}_{\text{acc}} \sim 0.02\text{--}0.03 M_{\odot} \text{yr}^{-1}$ near $R \sim 50$ pc while $\sim 0.1 M_{\odot} \text{yr}^{-1}$ near $R \sim 500$ pc. Figure 8 suggests that the radial profile of the mass accretion rate becomes flatter over time, in a way that the accretion rate near the CND increases with time. At $t = 300$ Myr, the CND formed in model B100 has gas mass $4 \times 10^5 M_{\odot}$, which is order of magnitude smaller than the observed CND masses $\sim 10^7 M_{\odot}$ in nearby active galaxies (Combes et al. 2019). We note, however, that the continued mass accretion with the rate of $\sim 0.01\text{--}0.1 M_{\odot} \text{yr}^{-1}$ is capable of producing $10^7 M_{\odot}$ CNDs within 0.1–1 Gyr. We also note that, because the magnetically driven mass accretion rate is proportional to $-B_R B_{\phi} = (B_R^2 + B_{\phi}^2)^{1/2} \sin(2\theta_p)/2$, the accretion rate would be higher if the magnetic fields are more loosely wrapped (i.e., larger pitch angle).

Tabatabaei et al. (2018) measured the magnetic field strength in 11 giant clumps in the nuclear ring of NGC 1097 and found a negative correlation between the star formation efficiency and magnetic field strength, suggesting that magnetic fields are inhibiting star formation in the nuclear ring. Figure 13(a) compares the observed average magnetic field strength of $62 \mu\text{G}$ (Tabatabaei et al. 2018) and depletion time of 5×10^8 yr (Prieto et al. 2019) with the results of our simulations. Based on our numerical results, the nuclear ring in NGC 1097 is in the regime where magnetic fields are dynamically important to suppression of star formation.

Our simulations demonstrate the intriguing possibility of star formation quenching in nuclear rings together with mass accretion to the center, both resulting from the growth of large-scale regular magnetic fields. However, it is still uncertain how the field strength and pitch angles depend on the underlying rotation curve and feedback physics as well as the magnetization of the inflowing gas, which models a bar-driven stream. These issues may be resolved by running more realistic simulations with improved physics. First of all, while the present work assumes that magnetic fields in the gas streams are kept constant, in real galaxies both the field strength and direction will vary with time, resulting in significant

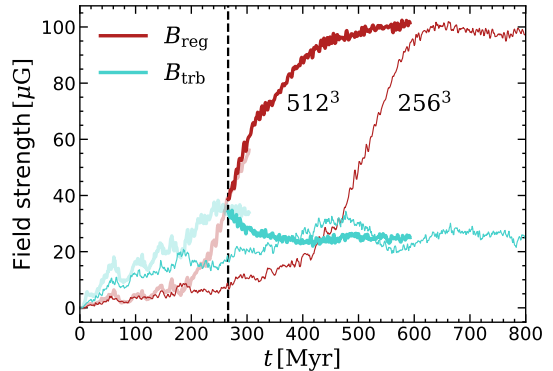


Figure 16. Evolution of the regular (brown) and turbulent (cyan) magnetic field strengths in the $\beta_{\text{in}} = 100$ model with an Alfvén speed ceiling applied in order to extend the simulation run time beyond that of model B100. Thick and thin lines correspond to the runs with 512^3 and 256^3 cells, respectively. The 512^3 run is restarted from model B100 (light-colored) at $t = 266$ Myr marked by the vertical dashed line, while the 256^3 run has an Alfvén ceiling applied throughout its evolution.

changes in the field strength and structure in nuclear rings and inward. In particular, the magnetic fields in the inflowing stream may change their polarity over a dynamical time at the bar end region and then be amplified in the ring. Reconnection with existing fields of the opposite polarity in the ring would then prevent excessive growth of the magnetic fields. To address this issue, it will be necessary to run global simulations of barred galaxies in which gas streams along dust lanes are modeled self-consistently by nonlinear interactions with a bar potential.

As Figure 10 shows, the regular magnetic fields B_{reg} in our simulations are still growing at the end of the runs, even though the turbulent component of the magnetic field has saturated. It is, however, of much interest to know how B_{reg} would evolve over longer timescales. For our standard simulations, following this late-time evolution is precluded by an extremely short timestep, as limited by the large Alfvén speed in locations where the density becomes low.⁸ However, by applying an artificial density floor to put a ceiling on the Alfvén speed of 10^3 km s^{-1} , we are able to restart our fiducial model B100 from $t = 266$ Myr and run up to $t = 600$ Myr, as shown in Figure 16. This figure shows that the magnetic fields saturate at $B_{\text{reg}} \sim 100 \mu\text{G}$ around $t \sim 520$ Myr. Additionally, we find that for a corresponding lower-

⁸ Large Alfvén speeds in our simulations occur in cones surrounding the z -axis above and below the CND, which have very low density but moderate magnetic field strength (see the right column of Figure 9).

resolution run, the saturation level of B_{reg} is the same, although saturation occurs at a later time (see Section 4.5). It is difficult to pinpoint what physical effect terminates the growth of B_{reg} , but radial spreading of the ring, nonlinear quenching due to small-scale helicity, and turbulent diffusion may all play a role (e.g. Brandenburg & Ntormousi 2022).

Our semi-global framework allows us to afford relatively high resolution of $\Delta x = 4$ pc uniformly across the entire domain such that the expansion of individual SN remnants is captured self-consistently. We note, however, that since the free-fall time of star-forming clumps in the ring is shorter than the SN delay time of ~ 4 Myr, early feedback in the form of radiation and stellar winds may affect gas dynamics and star formation efficiency of individual star-forming clumps significantly in extreme environments like nuclear rings. As a final caveat, we note that considering the low ionization fraction in densest star-forming clumps in nuclear rings, non-ideal terms in the induction equation that we have neglected in this study might potentially affect the growth of magnetic fields in the ring and therefore star formation and mass accretion flows.

1 We are grateful to the referee for an insightful report.
 2 The work of SM was supported by an NRF (National Re-
 3 search Foundation of Korea) grant funded by the Korean
 4 government (NRF-2017H1A2A1043558-Fostering Core
 5 Leaders of the Future Basic Science Program/Global
 6 Ph. D. Fellowship Program). The work of W.-T.K. was
 7 supported by the grant of National Research Founda-
 8 tion of Korea (2022R1A2C1004810). The work of C.-
 9 G.K. was supported in part by NASA ATP grant No.
 10 80NSSC22K0717. The work of ECO is partly supported
 11 by the Simons Foundation under grant 510940. Com-
 12 putational resources for this project were provided by
 13 Princeton Research Computing, a consortium including
 14 PICSciE and OIT at Princeton University, and by the
 15 Supercomputing Center/Korea Institute of Science and
 16 Technology Information with supercomputing resources
 17 including technical support (KSC-2021-CRE-0025).

Software: Athena (Stone et al. 2008), VisIt (Depart-
 ment Of Energy (DOE) Advanced Simulation & Com-
 puting Initiative (ASCI) 2011)

REFERENCES

- Allard, E. L., Knapen, J. H., Peletier, R. F., & Sarzi, M. 2006, MNRAS, 371, 1087, doi: [10.1111/j.1365-2966.2006.10751.x](https://doi.org/10.1111/j.1365-2966.2006.10751.x)
- Armillotta, L., Krumholz, M. R., Di Teodoro, E. M., & McClure-Griffiths, N. M. 2019, MNRAS, 490, 4401, doi: [10.1093/mnras/stz2880](https://doi.org/10.1093/mnras/stz2880)
- Athanassoula, E. 2005, MNRAS, 358, 1477, doi: [10.1111/j.1365-2966.2005.08872.x](https://doi.org/10.1111/j.1365-2966.2005.08872.x)
- Barkov, M. V., & Lyutikov, M. 2019, MNRAS, 489, L28, doi: [10.1093/mnrasl/slz124](https://doi.org/10.1093/mnrasl/slz124)
- Beck, R. 2015, A&A Rv, 24, 4, doi: [10.1007/s00159-015-0084-4](https://doi.org/10.1007/s00159-015-0084-4)
- Beck, R., Ehle, M., Shoutenkov, V., Shukurov, A., & Sokoloff, D. 1999, Nature, 397, 324, doi: [10.1038/16861](https://doi.org/10.1038/16861)
- Beck, R., Fletcher, A., Shukurov, A., et al. 2005, A&A, 444, 739, doi: [10.1051/0004-6361:20053556](https://doi.org/10.1051/0004-6361:20053556)
- Benedict, G. F., Smith, B. J., & Kenney, J. D. P. 1996, AJ, 112, 1318, doi: [10.1086/118104](https://doi.org/10.1086/118104)
- Bittner, A., Sánchez-Blázquez, P., Gadotti, D. A., et al. 2020, A&A, 643, A65, doi: [10.1051/0004-6361/202038450](https://doi.org/10.1051/0004-6361/202038450)
- Blackman, E. G., & Brandenburg, A. 2003, ApJL, 584, L99, doi: [10.1086/368374](https://doi.org/10.1086/368374)
- Boris, J. P. 1970, in Proc. Fourth Conf. on Numerical Simulation of Plasmas, ed. J. P. Boris & R. A. Shanny (Washington, D.C.: Naval Research Laboratory), 3
- Boulares, A., & Cox, D. P. 1990, ApJ, 365, 544, doi: [10.1086/169509](https://doi.org/10.1086/169509)
- Brandenburg, A., & Ntormousi, E. 2022, arXiv e-prints, arXiv:2211.03476, doi: [10.48550/arXiv.2211.03476](https://doi.org/10.48550/arXiv.2211.03476)
- Brandenburg, A., & Subramanian, K. 2005, PhR, 417, 1, doi: [10.1016/j.physrep.2005.06.005](https://doi.org/10.1016/j.physrep.2005.06.005)
- Butsky, I., Zrake, J., Kim, J.-h., Yang, H.-I., & Abel, T. 2017, ApJ, 843, 113, doi: [10.3847/1538-4357/aa799f](https://doi.org/10.3847/1538-4357/aa799f)
- Chen, C.-Y., & Ostriker, E. C. 2014, ApJ, 785, 69, doi: [10.1088/0004-637X/785/1/69](https://doi.org/10.1088/0004-637X/785/1/69)
- Childress, S., & Gilbert, A. D. 1995, Stretch, Twist, Fold: The Fast Dynamo (Heidelberg: Springer Berlin)
- Combes, F., García-Burillo, S., Audibert, A., et al. 2019, A&A, 623, A79, doi: [10.1051/0004-6361/201834560](https://doi.org/10.1051/0004-6361/201834560)
- Comerón, S., Knapen, J. H., Beckman, J. E., et al. 2010, MNRAS, 402, 2462, doi: [10.1111/j.1365-2966.2009.16057.x](https://doi.org/10.1111/j.1365-2966.2009.16057.x)
- de Sá-Freitas, C., Fragkoudi, F., Gadotti, D. A., et al. 2022, arXiv e-prints, arXiv:2211.07670, <https://arxiv.org/abs/2211.07670>
- Department Of Energy (DOE) Advanced Simulation, & Computing Initiative (ASCI). 2011, VisIt: Interactive Parallel Visualization and Graphical Analysis Tool, Astrophysics Source Code Library, record ascl:1103.007, <http://ascl.net/1103.007>

- Draine, B. T. 1978, *ApJS*, 36, 595, doi: [10.1086/190513](https://doi.org/10.1086/190513)
- Elmegreen, B. G. 1987, *ApJ*, 312, 626, doi: [10.1086/164907](https://doi.org/10.1086/164907)
- Elmegreen, B. G., Galliano, E., & Alloin, D. 2009, *ApJ*, 703, 1297, doi: [10.1088/0004-637X/703/2/1297](https://doi.org/10.1088/0004-637X/703/2/1297)
- Gadotti, D. A., Sánchez-Blázquez, P., Falcón-Barroso, J., et al. 2019, *MNRAS*, 482, 506, doi: [10.1093/mnras/sty2666](https://doi.org/10.1093/mnras/sty2666)
- Gadotti, D. A., Bittner, A., Falcón-Barroso, J., et al. 2020, *A&A*, 643, A14, doi: [10.1051/0004-6361/202038448](https://doi.org/10.1051/0004-6361/202038448)
- Gent, F. A., Mac Low, M.-M., Käpylä, M. J., & Singh, N. K. 2021, *ApJL*, 910, L15, doi: [10.3847/2041-8213/abed59](https://doi.org/10.3847/2041-8213/abed59)
- Glassgold, A. E., Galli, D., & Padovani, M. 2012, *ApJ*, 756, 157, doi: [10.1088/0004-637X/756/2/157](https://doi.org/10.1088/0004-637X/756/2/157)
- Gong, M., Ostriker, E. C., & Wolfire, M. G. 2017, *ApJ*, 843, 38, doi: [10.3847/1538-4357/aa7561](https://doi.org/10.3847/1538-4357/aa7561)
- Gressel, O., Elstner, D., Ziegler, U., & Rüdiger, G. 2008, *A&A*, 486, L35, doi: [10.1051/0004-6361:200810195](https://doi.org/10.1051/0004-6361:200810195)
- Hennebelle, P., & Inutsuka, S.-i. 2019, *Frontiers in Astronomy and Space Sciences*, 6, 5, doi: [10.3389/fspas.2019.00005](https://doi.org/10.3389/fspas.2019.00005)
- Heywood, I., Rammala, I., Camilo, F., et al. 2022, *ApJ*, 925, 165, doi: [10.3847/1538-4357/ac449a](https://doi.org/10.3847/1538-4357/ac449a)
- Indriolo, N., Geballe, T. R., Oka, T., & McCall, B. J. 2007, *ApJ*, 671, 1736, doi: [10.1086/523036](https://doi.org/10.1086/523036)
- Kim, C.-G., Kim, W.-T., & Ostriker, E. C. 2008, *ApJ*, 681, 1148, doi: [10.1086/588752](https://doi.org/10.1086/588752)
- Kim, C.-G., & Ostriker, E. C. 2015a, *ApJ*, 802, 99, doi: [10.1088/0004-637X/802/2/99](https://doi.org/10.1088/0004-637X/802/2/99)
- . 2015b, *ApJ*, 815, 67, doi: [10.1088/0004-637X/815/1/67](https://doi.org/10.1088/0004-637X/815/1/67)
- . 2017, *ApJ*, 846, 133, doi: [10.3847/1538-4357/aa8599](https://doi.org/10.3847/1538-4357/aa8599)
- Kim, J.-G., Kim, W.-T., Ostriker, E. C., & Skinner, M. A. 2017, *ApJ*, 851, 93, doi: [10.3847/1538-4357/aa9b80](https://doi.org/10.3847/1538-4357/aa9b80)
- Kim, J.-G., Ostriker, E. C., & Filippova, N. 2021, *ApJ*, 911, 128, doi: [10.3847/1538-4357/abe934](https://doi.org/10.3847/1538-4357/abe934)
- Kim, W.-T., & Elmegreen, B. G. 2017, *ApJL*, 841, L4, doi: [10.3847/2041-8213/aa70a1](https://doi.org/10.3847/2041-8213/aa70a1)
- Kim, W.-T., Kim, C.-G., & Ostriker, E. C. 2020, *ApJ*, 898, 35, doi: [10.3847/1538-4357/ab9b87](https://doi.org/10.3847/1538-4357/ab9b87)
- Kim, W.-T., & Ostriker, E. C. 2001, *ApJ*, 559, 70, doi: [10.1086/322330](https://doi.org/10.1086/322330)
- Kim, W.-T., Ostriker, E. C., & Stone, J. M. 2002, *ApJ*, 581, 1080, doi: [10.1086/344367](https://doi.org/10.1086/344367)
- Koyama, H., & Inutsuka, S.-i. 2002, *ApJL*, 564, L97, doi: [10.1086/338978](https://doi.org/10.1086/338978)
- Launhardt, R., Zylka, R., & Mezger, P. G. 2002, *A&A*, 384, 112, doi: [10.1051/0004-6361:20020017](https://doi.org/10.1051/0004-6361:20020017)
- Lemaster, M. N., & Stone, J. M. 2009, *ApJ*, 691, 1092, doi: [10.1088/0004-637X/691/2/1092](https://doi.org/10.1088/0004-637X/691/2/1092)
- Lopez-Rodriguez, E., Beck, R., Clark, S. E., et al. 2021, *ApJ*, 923, 150, doi: [10.3847/1538-4357/ac2e01](https://doi.org/10.3847/1538-4357/ac2e01)
- Ma, C., de Grijs, R., & Ho, L. C. 2018, *ApJ*, 857, 116, doi: [10.3847/1538-4357/aab6b4](https://doi.org/10.3847/1538-4357/aab6b4)
- Maciejewski, W. 2004, *MNRAS*, 354, 892, doi: [10.1111/j.1365-2966.2004.08254.x](https://doi.org/10.1111/j.1365-2966.2004.08254.x)
- Mazzuca, L. M., Knapen, J. H., Veilleux, S., & Regan, M. W. 2008, *ApJS*, 174, 337, doi: [10.1086/522338](https://doi.org/10.1086/522338)
- McKee, C. F., & Zweibel, E. G. 1995, *ApJ*, 440, 686, doi: [10.1086/175306](https://doi.org/10.1086/175306)
- Meier, D. S., Turner, J. L., & Hurt, R. L. 2008, *ApJ*, 675, 281, doi: [10.1086/524932](https://doi.org/10.1086/524932)
- Mestel, L., & Spitzer, L., J. 1956, *MNRAS*, 116, 503, doi: [10.1093/mnras/116.5.503](https://doi.org/10.1093/mnras/116.5.503)
- Moon, S., Kim, W.-T., Kim, C.-G., & Ostriker, E. C. 2021, *ApJ*, 914, 9, doi: [10.3847/1538-4357/abfa93](https://doi.org/10.3847/1538-4357/abfa93)
- . 2022, *ApJ*, 925, 99, doi: [10.3847/1538-4357/ac3a7b](https://doi.org/10.3847/1538-4357/ac3a7b)
- Neufeld, D. A., & Wolfire, M. G. 2017, *ApJ*, 845, 163, doi: [10.3847/1538-4357/aa6d68](https://doi.org/10.3847/1538-4357/aa6d68)
- Nishiyama, S., Hatano, H., Tamura, M., et al. 2010, *ApJL*, 722, L23, doi: [10.1088/2041-8205/722/1/L23](https://doi.org/10.1088/2041-8205/722/1/L23)
- Nogueras-Lara, F., Schödel, R., Gallego-Calvente, A. T., et al. 2020, *Nature Astronomy*, 4, 377, doi: [10.1038/s41550-019-0967-9](https://doi.org/10.1038/s41550-019-0967-9)
- Onishi, K., Iguchi, S., Sheth, K., & Kohno, K. 2015, *ApJ*, 806, 39, doi: [10.1088/0004-637X/806/1/39](https://doi.org/10.1088/0004-637X/806/1/39)
- Ostriker, E. C., & Kim, C.-G. 2022, *ApJ*, 936, 137, doi: [10.3847/1538-4357/ac7de2](https://doi.org/10.3847/1538-4357/ac7de2)
- Ostriker, E. C., McKee, C. F., & Leroy, A. K. 2010, *ApJ*, 721, 975, doi: [10.1088/0004-637X/721/2/975](https://doi.org/10.1088/0004-637X/721/2/975)
- Ostriker, E. C., & Shetty, R. 2011, *ApJ*, 731, 41, doi: [10.1088/0004-637X/731/1/41](https://doi.org/10.1088/0004-637X/731/1/41)
- Pakmor, R., Gómez, F. A., Grand, R. J. J., et al. 2017, *MNRAS*, 469, 3185, doi: [10.1093/mnras/stx1074](https://doi.org/10.1093/mnras/stx1074)
- Parker, E. N. 1955, *ApJ*, 122, 293, doi: [10.1086/146087](https://doi.org/10.1086/146087)
- Pillai, T., Kauffmann, J., Tan, J. C., et al. 2015, *ApJ*, 799, 74, doi: [10.1088/0004-637X/799/1/74](https://doi.org/10.1088/0004-637X/799/1/74)
- Piontek, R. A., & Ostriker, E. C. 2007, *ApJ*, 663, 183, doi: [10.1086/518103](https://doi.org/10.1086/518103)
- Prieto, M. A., Fernandez-Ontiveros, J. A., Bruzual, G., et al. 2019, *MNRAS*, 485, 3264, doi: [10.1093/mnras/stz579](https://doi.org/10.1093/mnras/stz579)
- Regan, M. W., Vogel, S. N., & Teuben, P. J. 1997, *ApJL*, 482, L143, doi: [10.1086/310717](https://doi.org/10.1086/310717)
- Rieder, M., & Teyssier, R. 2016, *MNRAS*, 457, 1722, doi: [10.1093/mnras/stv2985](https://doi.org/10.1093/mnras/stv2985)
- . 2017, *MNRAS*, 471, 2674, doi: [10.1093/mnras/stx1670](https://doi.org/10.1093/mnras/stx1670)
- Ruzmaikin, A., Sokolov, D., & Shukurov, A. 1988, *Nature*, 336, 341, doi: [10.1038/336341a0](https://doi.org/10.1038/336341a0)

- Sarzi, M., Allard, E. L., Knapen, J. H., & Mazzuca, L. M. 2007, *MNRAS*, 380, 949, doi: [10.1111/j.1365-2966.2007.12177.x](https://doi.org/10.1111/j.1365-2966.2007.12177.x)
- Seo, W.-Y., Kim, W.-T., Kwak, S., et al. 2019, *ApJ*, 872, 5, doi: [10.3847/1538-4357/aafc5f](https://doi.org/10.3847/1538-4357/aafc5f)
- Shimizu, T. T., Davies, R. I., Lutz, D., et al. 2019, *MNRAS*, 490, 5860, doi: [10.1093/mnras/stz2802](https://doi.org/10.1093/mnras/stz2802)
- Shlosman, I., Frank, J., & Begelman, M. C. 1989, *Nature*, 338, 45, doi: [10.1038/338045a0](https://doi.org/10.1038/338045a0)
- Shukurov, A., Sokoloff, D., Subramanian, K., & Brandenburg, A. 2006, *A&A*, 448, L33, doi: [10.1051/0004-6361:200600011](https://doi.org/10.1051/0004-6361:200600011)
- Skinner, M. A., & Ostriker, E. C. 2015, *ApJ*, 809, 187, doi: [10.1088/0004-637X/809/2/187](https://doi.org/10.1088/0004-637X/809/2/187)
- Sofue, Y. 2023, *MNRAS*, 518, 6273, doi: [10.1093/mnras/stac3137](https://doi.org/10.1093/mnras/stac3137)
- Sormani, M. C., & Barnes, A. T. 2019, *MNRAS*, 484, 1213, doi: [10.1093/mnras/stz046](https://doi.org/10.1093/mnras/stz046)
- Sormani, M. C., Tress, R. G., Glover, S. C. O., et al. 2020, *MNRAS*, 497, 5024, doi: [10.1093/mnras/staa1999](https://doi.org/10.1093/mnras/staa1999)
- Sormani, M. C., Sanders, J. L., Fritz, T. K., et al. 2022, *MNRAS*, 512, 1857, doi: [10.1093/mnras/stac639](https://doi.org/10.1093/mnras/stac639)
- Stone, J. M., & Gardiner, T. 2009, *NewA*, 14, 139, doi: [10.1016/j.newast.2008.06.003](https://doi.org/10.1016/j.newast.2008.06.003)
- Stone, J. M., Gardiner, T. A., Teuben, P., Hawley, J. F., & Simon, J. B. 2008, *ApJS*, 178, 137, doi: [10.1086/588755](https://doi.org/10.1086/588755)
- Sutherland, R. S., & Dopita, M. A. 1993, *ApJS*, 88, 253, doi: [10.1086/191823](https://doi.org/10.1086/191823)
- Tabatabaei, F. S., Minguez, P., Prieto, M. A., & Fernández-Ontiveros, J. A. 2018, *Nature Astronomy*, 2, 83, doi: [10.1038/s41550-017-0298-7](https://doi.org/10.1038/s41550-017-0298-7)
- Tress, R. G., Sormani, M. C., Glover, S. C. O., et al. 2020, *MNRAS*, 499, 4455, doi: [10.1093/mnras/staa3120](https://doi.org/10.1093/mnras/staa3120)
- Vainshtein, S. I., & Zel'dovich, Y. B. 1972, *Soviet Physics Uspekhi*, 15, 159, doi: [10.1070/PU1972v015n02ABEH004960](https://doi.org/10.1070/PU1972v015n02ABEH004960)
- Wada, K. 2004, in *Coevolution of Black Holes and Galaxies*, ed. L. C. Ho (Cambridge: Cambridge University Press), 186
- Yang, Y., Irwin, J., Li, J., et al. 2022, *ApJ*, 927, 4, doi: [10.3847/1538-4357/ac4ae7](https://doi.org/10.3847/1538-4357/ac4ae7)

APPENDIX

A. SEED MAGNETIC FIELDS

In the *Athena* code, magnetic fields are face-centered and are updated by the edge-centered electromotive force ($\propto \mathbf{v} \times \mathbf{B}$) using the constrained transport algorithm. Because our initial conditions have zero magnetic field at every *active* face, the only way to inject magnetic fields into the domain is by having non-zero electromotive forces at the boundaries. Even if \mathbf{B}_{in} is set parallel to \mathbf{v}_{in} for gas streams at the boundaries in our simulations, the fact that *Athena* defines the magnetic fields and velocity at the face centers and cell centers, respectively, enables $\mathbf{v}_{\text{in}} \times \mathbf{B}_{\text{in}} \neq 0$ at the domain boundaries, making the electromotive force nonzero and inducing seed magnetic fields in the active zones adjacent to the nozzles for an initial brief period of time.

To illustrate this, [Figure 17](#) diagrams a part of the computational domain near the positive- y boundary. The yellow shaded area indicates the ghost cells belonging to the upper nozzle and the white area marks the adjacent active cells. The blue arrows at the cell centers represent (v_x, v_y) of the stream at $t = 0$, which are non-zero only in the ghost cells and zero in the active cells. The red solid arrows at the cell faces indicate (B_x, B_y) of the stream at $t = 0$, which are also non-zero only in the ghost faces and zero in the active faces, while the red dashed arrows represent the cell-centered magnetic fields computed by averaging the neighboring face-centered fields. We note that the cell faces corresponding to the domain boundary are *active* (i.e., B_y at the border between the yellow and white areas is updated via [Equations \(1\) to \(5\)](#)). Because $B_y = 0$ initially at those boundary faces, the cell-centered B_y at the first ghost cells (adjacent to the active domain) is reduced by half, resulting in \mathbf{B}_{in} inclined to \mathbf{v}_{in} , the latter of which is set to [Equation \(14\)](#). As a result, non-vanishing electromotive forces are assigned to the edges of the outermost active cells which subsequently induce magnetic fields into the computational domain. We stress that this process occurs only for a few Myr in the very beginning: B_y at the outermost faces soon attains the same values as in the ghost faces to satisfy [Equation \(17\)](#). We also note that our initial conditions for the gas streams obey $\nabla \cdot \mathbf{B} = 0$ in the *active* domain, which is preserved by the constrained transport algorithm in *Athena*.

B. MAGNETIC ENERGY CONSERVATION

Here we consider the role of advection into the domain in the growth of magnetic energy in our simulations. We start with the equation for the rate of change of the total magnetic energy in the computational domain

$$\frac{dE_{\text{mag}}}{dt} = \int \frac{\partial}{\partial t} \left(\frac{B^2}{8\pi} \right) dV = \frac{1}{4\pi} \int \mathbf{B} \cdot [\nabla \times (\mathbf{v} \times \mathbf{B})] dV. \quad (\text{B1})$$

Integrating [Equation \(B1\)](#) by parts and applying the divergence theorem, one obtains

$$\frac{dE_{\text{mag}}}{dt} = \frac{1}{4\pi} \oint [(\mathbf{v} \times \mathbf{B}) \times \mathbf{B}] \cdot d\mathbf{A} - \frac{1}{4\pi} \int \mathbf{v} \cdot [(\nabla \times \mathbf{B}) \times \mathbf{B}] dV, \quad (\text{B2})$$

where $d\mathbf{A}$ denotes the area element. The first term in the right hand side of [Equation \(B2\)](#) represents the Poynting flux integrated over the domain boundaries, while the second term is the amount of work done by the fluid against the Lorentz force per unit time. It is evident that the first term vanishes when $\mathbf{v} \parallel \mathbf{B}$: there is no magnetic energy flux through the boundaries as long as the magnetic fields in the streams are parallel to the streaming velocity. One can further expand the cross products in the first term to write

$$\frac{dE_{\text{mag}}}{dt} = - \oint \mathbf{v} \cdot \mathbb{T} \cdot d\mathbf{A} - \oint \frac{B^2}{8\pi} \mathbf{v} \cdot d\mathbf{A} - \frac{1}{4\pi} \int \mathbf{v} \cdot [(\nabla \times \mathbf{B}) \times \mathbf{B}] dV. \quad (\text{B3})$$

In this form, the first and second term correspond to the work done by the Maxwell stress $\mathbb{T} \equiv B^2/(8\pi)\mathbb{I} - \mathbf{B}\mathbf{B}/(4\pi)$ at the boundaries and the advection of magnetic energy by the inflowing gas, respectively. Again, the two terms exactly cancel each other when $\mathbf{v} \parallel \mathbf{B}$.

As explained in [Appendix A](#), \mathbf{v} is not parallel to \mathbf{B} at the domain boundaries for the initial ~ 10 Myr, in which case the advection term is not offset by the Maxwell stress term, resulting in the growth of E_{mag} . One can estimate the maximum rate of the magnetic energy growth due to advection alone as

$$\frac{dE_{\text{mag,adv}}}{dt} = - \oint_{\text{nozzles}} \frac{B_{\text{in}}^2}{8\pi} \mathbf{v}_{\text{in}} \cdot d\mathbf{A} = - \frac{2k_{\text{B}}T_{\text{in}}}{\beta_{\text{in}}\mu_{\text{H}}m_{\text{H}}} \int_0^{\zeta_{\text{in}}} \rho_{\text{in}} \mathbf{v}_{\text{in}} \cdot \hat{\mathbf{y}} \cos^2 \left(\frac{\pi\zeta}{2\zeta_{\text{in}}} \right) 2\pi\zeta d\zeta \approx 0.6 \frac{k_{\text{B}}T_{\text{in}}\dot{M}_{\text{in}}}{\beta_{\text{in}}\mu_{\text{H}}m_{\text{H}}}, \quad (\text{B4})$$

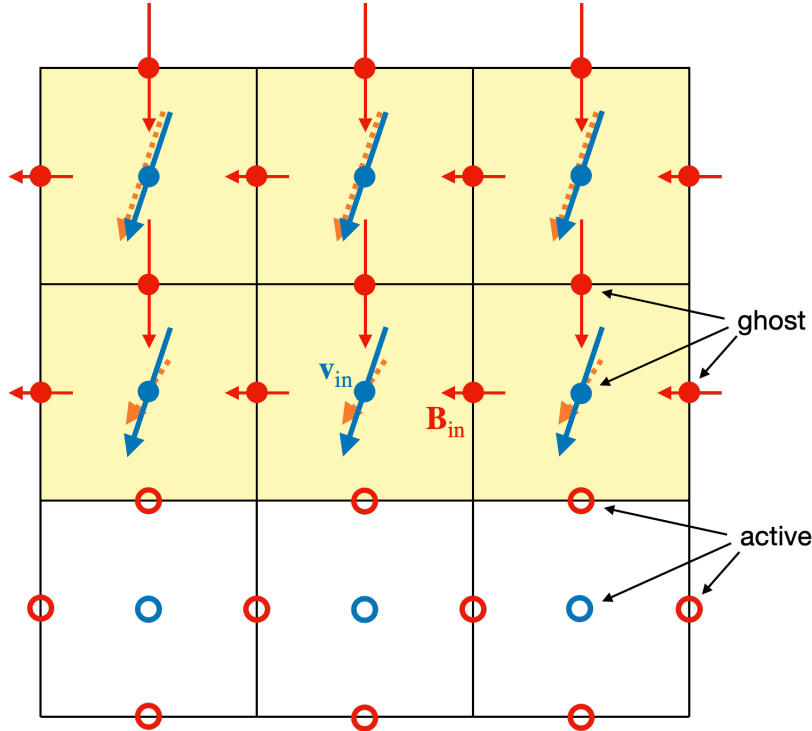


Figure 17. Illustration of the magnetic fields and velocity vectors in the ghost cells (shaded area) that belong to the nozzle at the positive y -boundary; the white area corresponds to the adjacent active cells. The blue arrows represent the velocity vectors, defined at cell centers. The solid and dashed arrows in red indicate the face- and cell-centered magnetic field vectors, respectively, with the latter computed from the former. Filled and open circles mark the ghost and active zones, respectively. See Appendix A for details.

where Equation (18) is used. For the parameters of model B100, $dE_{\text{mag,adv}}/dt \sim 1.4 \times 10^{49} \text{ erg Myr}^{-1}$. This suggests that the total magnetic energy that would be advected (barring the work done by the Maxwell stress) into the computational domain is $1.4 \times 10^{50} \text{ erg}$ for initial 10 Myr, which is a factor 3 smaller than the actual magnetic energy $E_{\text{mag}} = 4.3 \times 10^{50} \text{ erg}$ at $t = 10 \text{ Myr}$. In contrast, the total magnetic energy advected into the computational domain would be $4.2 \times 10^{51} \text{ erg}$ at the end of the run ($t = 300 \text{ Myr}$), which is about two orders of magnitude smaller than $E_{\text{mag}} = 7.2 \times 10^{53} \text{ erg}$ at the same epoch. Considering the work done by the Maxwell stress which tends to offset the magnetic energy growth by advection, the above result suggests that the actual magnetic energy advected through the nozzles should be negligible compared to what is generated by the last term in Equation (B3) via an MHD dynamo. We conclude that while the inflow nozzles provide seed magnetic fields, it is growth via dynamo activity rather than advection into the domain that is responsible for level of the magnetic energy at late times.

C. MASS ACCRETION RATES DUE TO MAXWELL AND REYNOLDS STRESSES

For gas to move radially inward while moving on an approximately circular orbit, it must lose angular momentum slowly. Here we derive the theoretical accretion rates due to the Maxwell and Reynolds stresses.

Multiplying the azimuthal component of Equation (2) by R yields

$$\frac{\partial(\rho R v_\phi)}{\partial t} + \nabla \cdot (\rho R v_\phi \mathbf{v} + R P \mathbf{e}_\phi) = -R \mathbf{e}_\phi \cdot (\nabla \cdot \mathbf{T}) - 2R \Omega_p \rho v_R - \rho \frac{\partial \Phi_{\text{tot}}}{\partial \phi}, \quad (\text{C5})$$

where \mathbf{e}_ϕ is the unit vector in the azimuthal direction. The second and third terms in the left hand side of Equation (C5) are the angular momentum flux due to macroscopic bulk fluid motion and the microscopic thermal motion of its constituent particles, respectively. The three source terms in the right hand side are the torque density due to the Lorentz force, the Coriolis force, and gravity, respectively. To focus on the radial mass inflow, we azimuthally average Equation (C5). Integrating the resulting equation in the vertical direction assuming the flux through the vertical

boundaries are negligible, one obtains

$$\frac{\partial \langle \rho R v_\phi \rangle}{\partial t} + \frac{1}{R} \frac{\partial \langle R^2 \rho v_R v_\phi \rangle}{\partial R} = -\frac{1}{R} \frac{\partial \langle R^2 T_{R\phi} \rangle}{\partial R} - 2R\Omega_p \langle \rho v_R \rangle, \quad (\text{C6})$$

where $\langle X \rangle \equiv (2\pi)^{-1} \iint X d\phi dz$ for any physical quantity X , and $T_{R\phi} = -B_R B_\phi / (4\pi)$ is the R - ϕ component of the Maxwell stress tensor. Note $\langle \rho \partial \Phi_{\text{tot}} / \partial \phi \rangle = \langle \rho \partial \Phi_{\text{self}} / \partial \phi \rangle \approx 0$ unless there is a systematic azimuthal offset between the density and self-gravitational potential. The magnetic torque term is due to the magnetic tension alone.

We decompose the velocity field into ordered and random components: $\mathbf{v} = v_{\text{circ}} \mathbf{e}_\phi + \mathbf{u}$, where $v_{\text{circ}} \equiv v_{\text{rot}} - R\Omega_p$ is the circular velocity in the rotating reference frame and \mathbf{u} is the random velocity. Substituting \mathbf{u} for \mathbf{v} and using the continuity equation (Equation (1)), Equation (C6) becomes

$$\frac{\partial \langle \rho R u_\phi \rangle}{\partial t} - \frac{\dot{M}_{\text{acc}}}{2\pi R} \frac{\partial (R v_{\text{circ}})}{\partial R} + \frac{1}{R} \frac{\partial \langle R^2 \rho u_R u_\phi \rangle}{\partial R} = -\frac{1}{R} \frac{\partial \langle R^2 T_{R\phi} \rangle}{\partial R} - 2R\Omega_p \langle \rho u_R \rangle, \quad (\text{C7})$$

where $\dot{M}_{\text{acc}} \equiv -2\pi R \langle \rho u_R \rangle$ is the mass accretion rate at radius R . Assuming a quasi-steady state (which turns out to be the case in our simulations) and neglecting the Coriolis term which is unimportant for small R , Equation (C7) is simplified to

$$\dot{M}_{\text{acc}} \approx \dot{M}_{\text{M}} + \dot{M}_{\text{R}}, \quad (\text{C8})$$

where \dot{M}_{M} and \dot{M}_{R} are the mass accretion rates due to the Maxwell and Reynolds stress, defined in Equation (21). Figures 7 and 8 show that the mass accretion in our simulations is dominated by \dot{M}_{M} , that is, magnetic tension.